Molecular fingerprints of star formation throughout the Universe : a space-based infrared study

Lahuis, F.

Citation

Lahuis, F. (2007, May 9). *Molecular fingerprints of star formation throughout the Universe : a space-based infrared study*. Retrieved from https://hdl.handle.net/1887/11950

Chapter 5

c2d *Spitzer* IRS Spectra of Disks around T Tauri Stars III. [Ne II] and H_2 gas-phase lines

Abstract

We present a survey of mid-infrared gas-phase lines, in particular the pure rotational H_2 and atomic fine structure lines, toward a sample of 76 circumstellar disks around low mass pre-main sequence stars from the *Spitzer* ”From Molecular Cores to Planet Forming Disks” (c2d) legacy program. We report the first detections of [Ne II] toward T Tauri stars in $\gtrsim 20$ % of our sources. The observed [Ne II] line fluxes and upper limits are consistent with [Ne II] excitation in an X-ray irradiated disk around stars with X-ray luminosities $L_\mathrm{X} = 10^{29} - 10^{31}\,\mathrm{erg\,s^{-1}}$. No compact H_2 0-0 S(0) and S(1) disk emission is detected giving upper limits on the warm ($T \sim 100 - 200$ K) gas mass of typically a few Jovian masses. Emission of hot ($T \gtrsim 500$ K) gas is observed through the H_2 0-0 S(2) and/or S(3) lines toward ~ 7 % of our sources. Of these all but one show [Ne II] emission suggesting a possible common heating and excitation mechanism through X-rays or EUV. Analysis of the spatial profiles together with mini-maps for selected sources shows that this emission is compact and associated with the disk. The upper limits on the H_2 lines are consistent with the amount of warm (> 100 K) gas and H_2 excitation in recent T Tauri disk models that include gas heating by stellar radiation. The detected S(2) and S(3) line fluxes are, however, higher by more than an order of magnitude than those found in recent disk models, even when X-ray and excess UV radiation is included. Similarly the [Ne II]/H_2 0-0 S(2) ratios for these sources are lower than predicted, consistent with the presence of an additional hot molecular gas component not included in current disk models. No [S I] or [Fe II] is detected down to $\sim 10^{-6}\,L_\odot$ while [Fe I] has been detected toward ~ 8 % of the sources at $\sim 10^{-5} - 10^{-4}\,L_\odot$ indicating the presence of gas-rich disks with masses of at least $0.1 M_\mathrm{J}$. Oblique shocks due to stellar winds interacting with the disk can explain many aspects of the hot gas emission, but they are inconsistent with the non-detection of [S I] and [Fe II] lines.

Lahuis, F., van Dishoeck, E. F., Blake, G. A., Evans N. J. II, Kessler-Silacci, J. E., & Pontoppidan, K. M., 2007, submitted to ApJ

5.1 Introduction

Circumstellar disks are a natural and important phenomenon in low-mass star formation. The ability to trace the evolution of the disk dust and gas content is crucial to understanding their chemistry and physics and the formation of planets. Observed disks reveal a large source to source variation and suggest a complex evolution from young gas-rich disks to tenuous debris disks. Disk geometries are observed to range from almost flat to strongly flaring disks (Dullemond & Dominik, 2004), and disks with large inner cavities are found (Calvet et al., 2002; Bouwman et al., 2003; Forrest et al., 2004; Brown & et al., 2007). Observations of silicates and spectral energy distributions (SEDs) present evidence for grain growth and settling of large grains to the disk midplane (van Boekel et al., 2003; D'Alessio et al., 2006; Kessler-Silacci et al., 2006). Different degrees of grain heating and radial mixing in the disks (van Boekel et al., 2005), and varying PAH abundances affect the heating of the upper layers of the disk (Habart et al., 2006; Geers et al., 2006). Most of these disk properties are derived from infrared solid-state features and from near-infrared to millimeter continuum observations and associated SED modeling. However, such data give little information about the gas in the disk.

Gas plays an important role in the structure and evolution of disks, including the temperature and density gradients, chemistry, dust dynamics, and eventually the formation of gas-rich and gas-poor planets (Gorti & Hollenbach, 2004). Observational diagnostics of the physical conditions of the gas, in particular its mass and temperature, are therefore highly relevant to studies of disk evolution and planet formation. Central questions are how the gas in the disk is dissipated, what drives the disk heating and gas clearing, and what the associated timescales are. The small number of observed transitional objects between the classical T Tauri phase (large Hα equivalent width, thought to be accreting) and the weak-line T Tauri phase (small Hα, non accreting), both with massive optically thick disks, and the more evolved phase with optically thin or no disks, suggests that disk clearing timescales are short (few$\times 10^5$ yr) compared to the disk lifetime of a few Myr (Cieza & et al., 2007; Haisch et al., 2001). In addition, combined near-infrared (IR), mid-IR, and millimeter observations imply that the disk clearing happens nearly simultaneously across the disk (see e.g. Kenyon & Hartmann, 1995; Hartmann et al., 2005; Takeuchi et al., 2005). Alexander et al. (2006) present a new evolutionary model combining viscous evolution with photoevaporation of the disk to address these issues. In this mechanism, the disk is cleared through an evaporative flow originating from the disk surface layers as a result of UV and/or X-ray heating (see e.g. Hollenbach et al., 2000; Clarke et al., 2001; Kamp & Dullemond, 2004; Dullemond et al., 2007). Information about the temperature and mass of the warm gas and constraints on the disk heating processes are vital for advancing the current models.

Models of gas heating include UV and X-ray radiation from the star itself as well as possible excess radiation due to accretion (e.g. Jonkheid et al., 2004; Gorti & Hollenbach, 2004; Kamp & Dullemond, 2004; Nomura & Millar, 2005; Jonkheid et al., 2007). The resulting gas temperatures in the surface layers out to large radii are significantly higher than those of the dust as a result of the photoelectric effect on small grains and PAHs. Gas temperatures may reach values of up to a few thousand K. Once grains have grown to μm sizes or larger, however, the gas temperature is significantly decreased unless PAHs are still present (Jonkheid et al. 2004, 2006, 2007). Nomura & Millar (2005) include explicitly the excitation of H_2 by UV and collisions for a disk around a T Tauri star with and without excess UV and make predictions for line intensities which can be tested against observations. Glassgold et al. (2007) have studied the case of X-ray heating and have shown that the ionized neon fine-structure line emission may provide unique tracers of X-ray heating in the disk surface since neon cannot be photoionized by radiation with energies below 13.6 eV.

Observational studies of the gas and its temperature have mostly been limited to the hot inner disks, the low-density upper atmospheres, and the cold outer regions of disks. None of these trace the bulk of the disk gas. High-resolution CO v=1–0 vibration-rotation lines at 4.7 μm (Najita et al., 2003; Brittain et al., 2003; Blake & Boogert, 2004) show gas with temperatures $\sim 1000 - 3000\,\mathrm{K}$ in the surface layers out to $\sim 1\,\mathrm{AU}$. H_2O emission from SVS 13 (Carr et al., 2004) and molecular absorption of C_2H_2, HCN, and CO_2 in the disk of IRS 46 (Lahuis et al., 2006b) also indicate hot temperatures in the inner few AU of several hundred K. Bary et al. (2003) detected H_2 2.1μm 1–0 S(1) emission most likely resulting from hot fluorescently excited gas from the low-density upper atmospheres out to radii of a few$\times$10 AU. In contrast, millimeter CO surveys probe the cold gas throughout the outer disk where the dust is optically thin (e.g. Koerner & Sargent, 1995; Duvert et al., 2000; Thi et al., 2001; Dutrey et al., 2003; Dent et al., 2005). Its use as a gas mass tracer is however limited as a result of both strong photodissociation at low extinction and freeze-out in the disk interior. Gas temperature determinations range from <20 K near the midplane (Dartois et al., 2003; Piétu et al., 2007) to 40 K or higher in the intermediate and surface layers (van Zadelhoff et al., 2001; Qi et al., 2006).

The mid-IR H_2 and atomic fine structure lines are best suited as direct tracers of the warm (~100 K) gas in the intermediate zones of disks at radii of a few AU out to several tens of AU, i.e., the planet-forming zones of disks. The Infrared Space Observatory (ISO) provided the first opportunity to probe this warm gas in disks around Herbig Ae and T Tauri stars. Thi et al. (2001) suggested that large amounts ($\sim 0.01 - 100\,\mathrm{M}_J$) of gas could reside in disks around young T Tauri stars, but this has not been confirmed by subsequent ground-based observations (Richter et al., 2002; Sheret et al., 2003; Sako et al., 2005).

The sensitive InfraRed Spectrograph (IRS) (Houck et al., 2004) on board the *Spitzer* Space Telescope (Werner et al., 2004) brings the detection of these lines within reach for young solar mass stars in nearby star forming regions. The combination of high sensitivity, moderate spectral resolution $R = \lambda/\Delta\lambda = 600$, and modest spatial resolution makes *Spitzer* well suited for the direct study of the gas in and around low-mass young stars in nearby ($\lesssim 300\,\mathrm{pc}$) clouds through the mid-IR lines of various species.

We present here an overview of gas-phase lines detected in disks observed in the *Spitzer* legacy program "From Molecular Cores to Planet Forming Disks" ("Cores to Disks" or c2d) (Evans et al., 2003), which has collected a large sample of IRS spectra toward sources in the nearby Chamaeleon, Lupus, Perseus, Ophiuchus, and Serpens star-forming regions. High-S/N 5-38 μm spectra have been obtained for 226 sources at all phases of star and planet formation up to ages of ~5 Myr. From this sample, 76 disk sources, identified by showing either the 10 or 20 μm silicate bands in emission, have been selected. In §5.2 and §5.3 the source selection and data reduction are explained. In §5.4 the observed atomic fine-structure and H_2 emission lines and the derived parameters are presented. In §5.5 the results are reviewed in the context of currently available disk models. This paper forms a complement to the searches for the mid-infrared lines of H_2 and other species toward more evolved disks studied in other *Spitzer* (legacy) programs (Hollenbach et al., 2005; Pascucci et al., 2006).

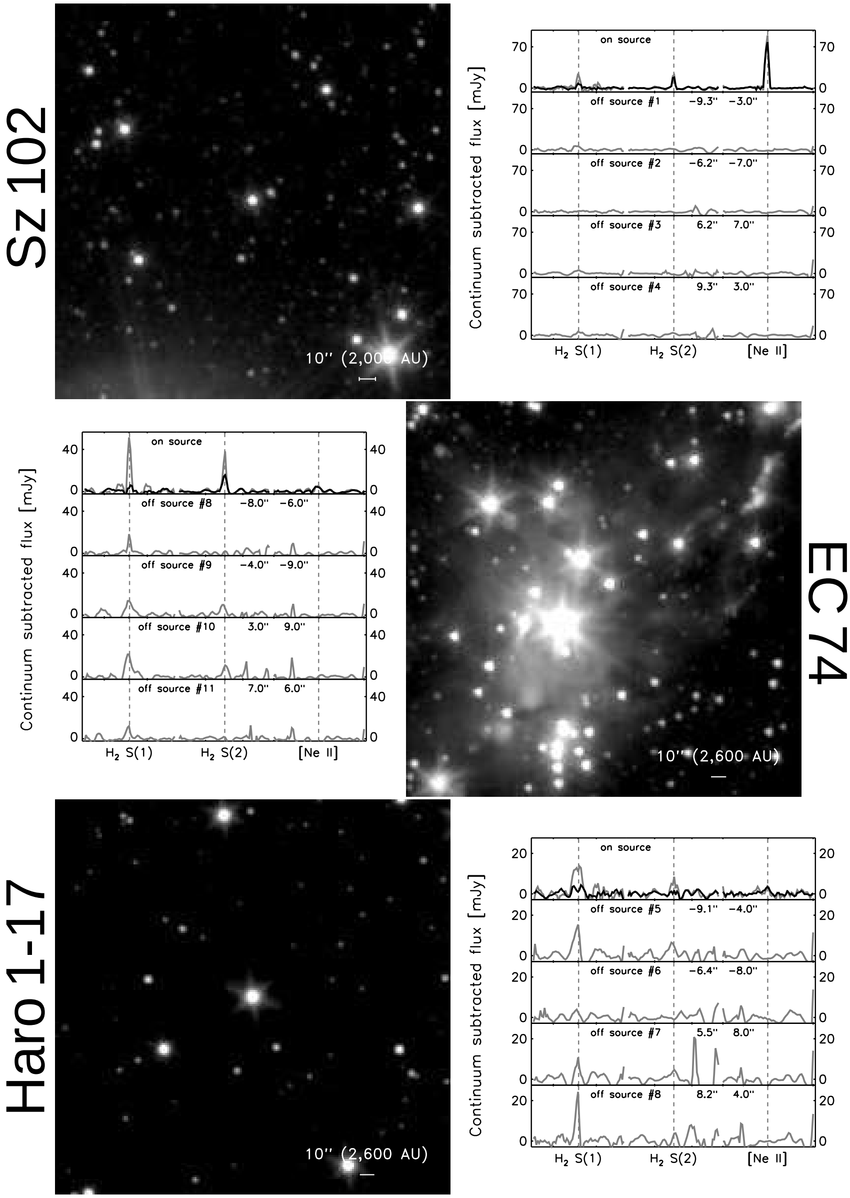

Figure 5.1 Observations of H_2 0-0 S(1), S(2), and [Ne,II] emission observed on and off source toward Sz 102, EC 74, and Haro 1-17. The on source observations were observed in the c2d first-look program, the follow up off source observations in the second look program (see §5.2). The images show *Spitzer* IRAC images at 4.5 μm (including the high excitation H2 S(9), S(10) and S(11) lines) with the sources in the middle. The gray lines in the spectra show the total (compact source plus extended component) observed emission. The black lines the source emission after correction for the extended component. Note that for the off source observations no compact source could be identified by the optimal extraction routine and consequently no compact source emission is plotted. Although the S/N in the off source positions is often poor, it illustrates the problem of extended and non-uniform H_2 emission. The [Ne II] is almost always limited to the source itself.

5.2 Observations

The data presented in this study were selected from the sample of IRS spectra observed within the *Spitzer* c2d legacy program. The c2d IRS program consists of two programs of comparable size, referred to as the first- and second-look programs. The first-look program (PID #172) was restricted primarily to known low-mass young stars, embedded YSOs and pre-main-sequence stars with disks with masses $M < 2\ M_\odot$ and ages $\lesssim$5 Myr, and a sample of background stars. A few Herbig Ae stars are included as well. The c2d source selection criteria were defined to be complementary to those of the *Spitzer* legacy program "The Formation and Evolution of Planetary Systems" (FEPS, Meyer et al., 2002). The second-look program (PID #179) was, for the most part, devoted to IRS follow-up spectroscopy of sources discovered in the IRAC and MIPS mapping surveys, including a newly discovered cluster of young stars in Serpens (Harvey et al., 2006). For all first-look observations, the integration times for the short-high (SH) and long-high (LH) modules ($R = 600$, 10–37 μm) were chosen such that theoretical signal to noise ratios (S/Ns) of at least 100 and 50 on the continuum were obtained for sources brighter and fainter than 500 mJy, respectively. Deeper integrations were not feasible within the c2d program. Spectra taken using the short-low (SL) or long-low (LL) modules ($R = 60 - 120$, 5-14 μm and 14-38 μm respectively) always reach theoretical S/N ratios greater than 100. For the second-look IRS targets similar S/N limits were obtained wherever possible. However, since the second-look contained a number of very weak sources (down to a few mJy) this was not always achieved.

5.2.1 Source selection

The sources presented in this paper were all selected to show either of the $10\,\mu$m or $20\,\mu$m silicate bands in emission. A total of 76 sources were chosen; see Kessler-Silacci et al. (2006) for the 47 first-look disk sources with silicate emission. This selection excludes most edge-on disk sources ($i \gtrsim 65$ degrees) such as CRBR 2422.8-3423 (Pontoppidan et al., 2005), IRS 46 (Lahuis et al., 2006b) and the 'Flying Saucer' (Pontoppidan et al., 2007), with the exception of the high inclination sources EC82 (Pontoppidan & Dullemond, 2005) and VV Ser which are included in this paper. Gas-phase lines toward edge-on disk sources will be discussed in a separate paper together with the embedded class 0 and I sources (Lahuis et al., in prep.). The selected sources are listed in Table 5.1 which gives the basic observing and source parameters, e.g. the adopted distances.

5.2.2 SH mini maps

In an early phase of the c2d project molecular hydrogen and [Ne II] lines were detected toward some of the c2d sources. As part of the second-look program, follow-up mini-maps were taken using the SH module to check for extended emission at offsets positions of $\sim$10-15$''$ with respect to the sources. Five maps were defined to include off source observations around eight sources. Three of these are disk sources included in our sample, Sz 102 (Krautter's star), Haro 1-17, and EC74. Figure 5.1 shows the observed H_2 0-0 S(1), S(2), and [Ne II] emission from the first-look on source observations together with the off source observations from the second-look mini maps. The maps show that most of the H_2 emission is extended, especially for the S(1) line. However, fine-structure lines are usually seen to be limited to the source itself. Subsequent results using the c2d optimal extraction procedure (see §5.3.1) confirm the conclusions drawn from the analysis of the mini-maps.

The SH maps are not complete since the time allocated for c2d spectroscopy did not allow to observe fully sampled maps. The prime purpose of the maps is to confirm the presence or absence of extended emission. More extended mapping observations will be required to study the detailed spatial distribution and extent of the large scale emission component.

5.3 Data reduction

The c2d reduction pipeline (see Chapter 3 and Lahuis et al., 2006a) was used to reduce the IRS data, starting from the S13 and S14 archive data. The same c2d pipeline products as included in the final c2d Legacy data delivery were used for the spectral line analysis (see §5.3.3). Most of the analysis focused on the SH and LH data, since the SL and LL data are generally limited by the low line/continuum ratio. The SL data were included and used to search for higher-excitation H_2 0-0 lines, in particular the S(3) transition.

5.3.1 Separating disk and cloud emission – optimal extraction

A major concern when studying emission lines from young stellar objects (YSOs) is the possible contribution of extended (envelope or local cloud) emission in the sometimes complex star forming regions. The spatial distribution of the emission, both in the continuum and in spectral lines, often prohibits the use of 'sky' observations alone to correct for extended emission components. For this reason the c2d team has developed an optimal extraction algorithm for IRS pointed observations (see §3.2.2.2).

The *Spitzer* diffraction limited beam is $\sim 4-5$ arcsec for the SH module (10-19.5 μm) and $\sim 7-10$ arcsec for the LH module (19-37 μm). At a distance of 100 parsec this corresponds to physical sizes of ~400-500 AU and ~700-1000 AU, respectively. The clouds observed in the c2d program are located at distances ranging from 125 parsec (Ophiuchus) to 260 parsec (Serpens) increasing the physical area observed. The full IRS aperture in the SH and LH spatial direction is $\sim 2.5-3$ times larger than the beam size. At the observed cloud distances this means that the aperture probes physical scales of several thousand AU. This makes it ideally suited for detecting cold or shocked H_2 emission from the extended (remnant) envelope, outflows, or the diffuse local cloud emission. For the disk sources studied in this work however the local cloud emission will potentially confuse the compact disk emission. Distinguishing between compact (disk) and extended (remnant envelope, outflow, or diffuse cloud) emission is therefore of vital importance for studying the emission lines originating in the circumstellar disks. The optimal PSF extraction developed by the *Spitzer* c2d legacy team (see Chapter 2 in praticular §3.2.2.2 Lahuis et al., 2006a) allows separation of the two components for all sources. The mini-maps (see §5.2.2) observed around selected sources confirm the results of the optimal extraction. See Figure 5.1 for an example of extended H_2 emission but compact [Ne II] emission. Other examples include Figures 3 and 4 in Geers et al. (2006) for separating extended cloud and compact disk PAH emission.

The c2d legacy data are accessible at `http://ssc.spitzer.caltech.edu/legacy/c2dhistory.html`.

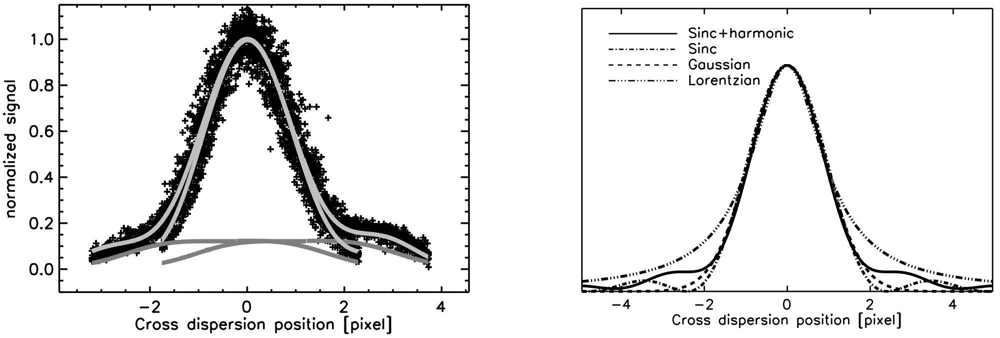

Figure 5.2 Illustration of the *Spitzer* IRS cross dispersion profile used in the optimal extraction (see §5.3.1). The left plot shows a fit to the IRS SH order 11 data of GW Lup, a source with a moderate but clear sky component in the IRS spectra. The rsc data (bcd data before flatfielding) of both dither position (black plusses) is shown, normalized, collapsed along the dispersion direction, and corrected for the cross dispersion dither offsets. Overplotted is the combined fit of the source profile plus the extended emission in gray and the extended emission in dark gray. The shape of the extended emission reflects the IRS flatfield of the (for this source) assumed uniform extended emission. The right plot shows a comparison of an IRS PSF profile (Sinc plus harmonics) compared to the profiles of an undistorted Sinc, a Gaussian, and a Lorentzian profile with the same FWHM. Note the significant variation in the strength and shape of the profile wings. The correct characterization of both the width and the wings of the profile for all IRS orders is essential for extracting the proper source and sky spectra.

The optimal extraction uses an analytical cross-dispersion point spread function (PSF) for the source profile plus an extended emission component to fit to the observed cross dispersion echelle data, see Figure 5.2 for an example. The characterization of the PSF is done using a suite of high S/N calibrator stars. A flux calibration tuned to the optimal extraction is derived from the same calibrator stars using Cohen templates and MARCS models provided by the *Spitzer* Science Center (Decin et al., 2004). The optimal extraction returns a total flux value (the source flux plus extended emission in the IRS beam) and the estimate of the extended emission component. Error estimates are derived for both the total emission and the extended emission component. The S/N of the extended emission component can vary significantly. It depends on the quality of the raw aperture data and on deviations of the extended emission from the assumed uniformity across the IRS slit. Therefore, care has to be taken when subtracting the extended emission from the total flux signal to retrieve the compact source emission. In some cases, a fit to the extended continuum and line emission is used to avoid adding in surplus noise from the often more noisy extended emission component. The uncertainty on the fit to the extended emission is then propagated into the error of the compact source signal.

5.3.2 1-D spectra

After extraction, the 1-D spectra are corrected for instrumental fringe residuals (Lahuis & Boogert, 2003), order matching is applied, and an estimate of the pointing error is obtained for the compact source component. Pointing offsets up to a few arcsec can have a significant impact on the derived fluxes of lines observed with the SH and SL modules, e.g. H_2 0-0 S(1), S(2), [Ne II], and [Ne III]. For example, dispersion offsets within the nominal 3σ pointing uncertainty of *Spitzer* ($\sim 1''$ for medium accuracy peakup) can lead to SL and SH flux losses up to $\sim$ 10% depending on wavelength. For all targets, a combination of either the SH, LH, and SL, SH and LH, or SH and SL modules is available. This in principle allows a correction of the pointing related flux losses with an accuracy given by the S/N of the data in the module overlap areas. A detailed description of the c2d pipeline (including extraction, defringing, pointing correction) and the c2d legacy products is given in the "c2d Spectroscopy Explanatory Supplement" (Lahuis et al., 2006a).

5.3.3 Spectral analysis

The SH and LH modules of the IRS instrument cover the positions of the three lowest pure rotational lines of H_2 and emission of [Ne II] (12.8 μm), [Ne III] (15.55 μm), [Fe I] (24 μm), [Fe II] (17.9 and 26.0 μm), [S I] (25.25 μm), [S III] (18.7 μm), and [Si II](34.8 μm) at a resolving power of $R = \lambda/\Delta\lambda = 600$. Line fitting and flux integration is done using routines from OSIA.

As discussed in §5.3.1, the extended emission component, both in the continuum and the spectral line, is subtracted from the spectrum prior to line fitting. Uncertainty estimates, as listed in Table 5.2, are derived from the residuals after line fitting, or, in the absence of a spectral line, using the line width derived from the instrumental resolution. The uncertainty derived from the extended emission is added into the uncertainty estimate of the source component. As a result, the 1-σ uncertainty estimates can vary widely for sources with a similar continuum flux and integration time. This may for example be the result of the presence of artifacts resulting from hot pixels or small variations in the extended emission which are not accounted for in the spectral extraction which assumes a constant extended emission component.

Typical mean 3σ uncertainties prior to subtraction of the extended component for the high resolution modules range from $\sim 1 \times 10^{-16} - 2 \times 10^{-15}$ $\mathrm{erg\,cm^{-2}\,s^{-1}}$ with extremes of $\sim 5 \times 10^{-17}$ $\mathrm{erg\,cm^{-2}\,s^{-1}}$ and $\sim 1 \times 10^{-14}$ $\mathrm{erg\,cm^{-2}\,s^{-1}}$. The uncertainties are comparable to those from Pascucci et al. (2006) for FEPS observations using on source integration times similar to those used for the c2d sample.

5.4 Results

5.4.1 Atomic fine-structure lines: Neon

Of all the atomic fine structure lines covered by the SH and LH modules, the [Ne II] 12.8μm transition is most convincingly detected and shows the strongest source emission. The higher excitation [Ne III] 15.5μm line is not detected toward any of the sources in our sample. Figure 5.3 shows all [Ne II] lines detected at 3σ or more; see also Fig. 1 of Geers et al. (2006) for the [Ne II] 12.8 μm line toward T Cha. Plotted in Figure 5.3 is the total continuum-subtracted observed [Ne II] emission in gray and the compact source emission after correction for extended line emission in black. Taken together, [Ne II] emission is observed in the spectra of 17 T Tauri sources and one Herbig Ae/Be

---

OSIA is a joint development of the ISO–SWS consortium. Contributing institutes are SRON, MPE, KUL and the ESA Astrophysics Division. `http://sws.ster.kuleuven.ac.be/osia/`

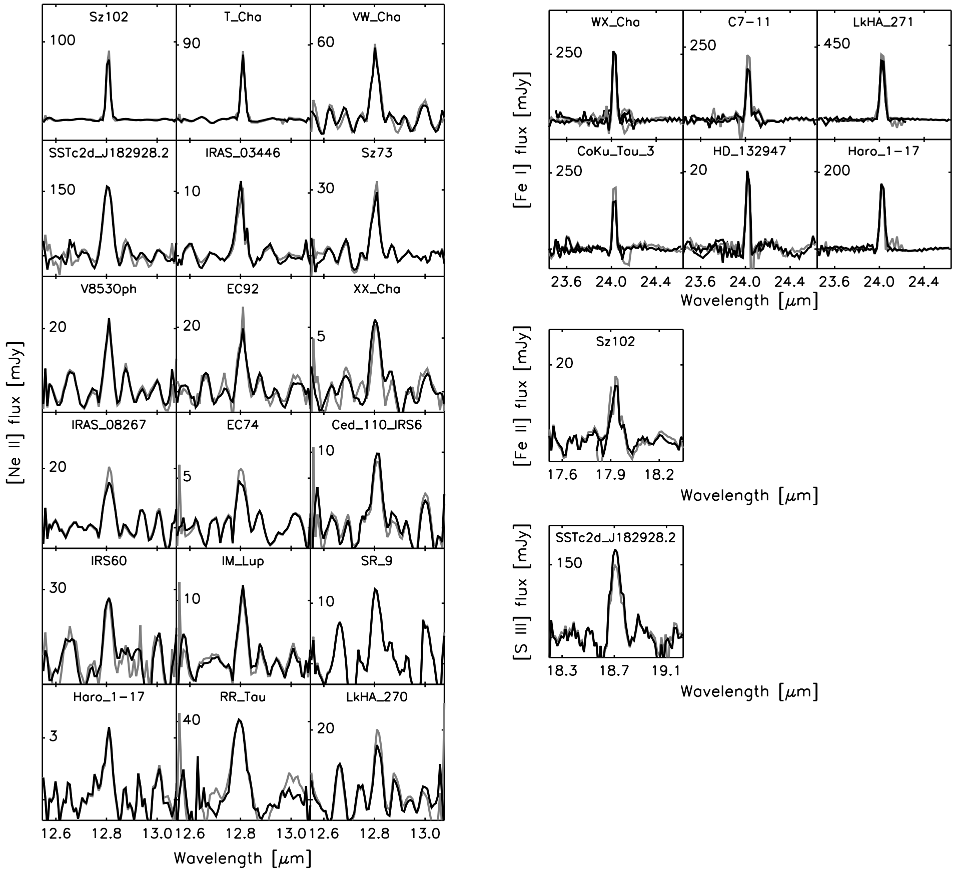

Figure 5.3 Detections of [Ne II], [Fe I], [Fe II], and [S III] at the 3σ level or more toward the c2d sample of T Tauri stars with disks. Of all the H_2 and atomic fine structure lines [Ne II] and [Fe I] are most convincingly detected toward $\gtrsim$ 20 % and $\sim$ 8 % of the sources respectively. Plotted in gray is the total observed emission (compact source + extended component) and in black the emission after correction of the estimated sky component. None of the sources show a significant extended component in any of the atomic fine structure lines.

star (RR Tau) ($\gtrsim$ 20 % of the sample). These are the first reported detections of [Ne II] toward disks around classical T Tauri stars. The optimal extraction method, together with the limited mini-maps (§5.2.2 and Fig. 5.1), show that the emission is indeed associated with the source itself.

The observed line fluxes and upper limits of [Ne II] and [Ne III] are listed in columns 8 and 9 of Table 5.2. When line fluxes are compared (observed or with models) the line strength is converted to solar luminosities since the sample is observed toward sources from multiple clouds and compared to model predictions using different assumed distances. Figure 5.4 shows the distribution of the observed line strengths (solid bars) and upper limits (hatched bars).

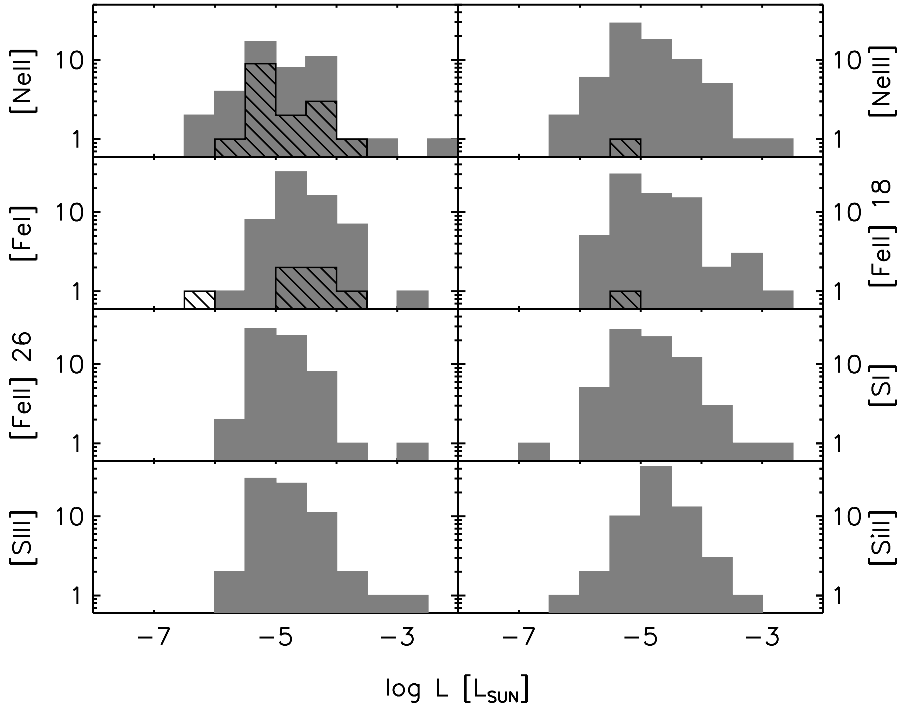

Figure 5.4 Observed line strengths (hatched bars) and upper limits (solid gray bars) of the major atomic lines. Included with vertical lines are model predicted line strengths for [Ne II] and [Ne III] by Glassgold et al. (2007). The model incorporates UV and X-ray heating of the circumstellar disk. The two lines represent two extreme thermal models, X-ray heating dominant (dotted line) or mechanical heating dominant (dashed line).

5.4.2 Atomic fine-structure lines: Other species

[Fe I] at 24μm is the only other species besides [Ne II] with clear detections toward six sources ($\sim$ 8 % of the sample). Of the other atomic lines there is one detection of [Fe II] at 18μm and one of [S III] at 18.7 μm, in different sources. [S I] at 25 μm, [Fe II] at 26μm, and [Si II] at 34 μm are not detected. The derived line fluxes and upper limits are listed in columns $9-14$ in Table 5.2. The detected lines are plotted in Figure 5.3 whereas Figure 5.4 shows the distribution of the observed line strengths.

5.4.3 Molecular hydrogen

H_2 emission is detected toward a small number of sources. Figure 5.5 shows the observed H_2 0-0 S(2) and S(3) emission lines detected at 3σ or more. The total (compact and extended line emission) observed H_2 emission (in gray) and the emission after subtraction of the extended line emission (in black) are shown. The H_2 0-0 S(0) and S(1) lines are seen toward some sources such as HD 132947 and Sz 102 (Fig. 5.1) but they are always found to be extended, and hence not considered here. Neither S(0) nor S(1) are seen toward HD 135344 and HD 163296. The 3σ upper limits for HD 135344 are a factor of $\sim 2-3$ lower than the tentative detections in Thi et al. (2001), while for HD 163296 the

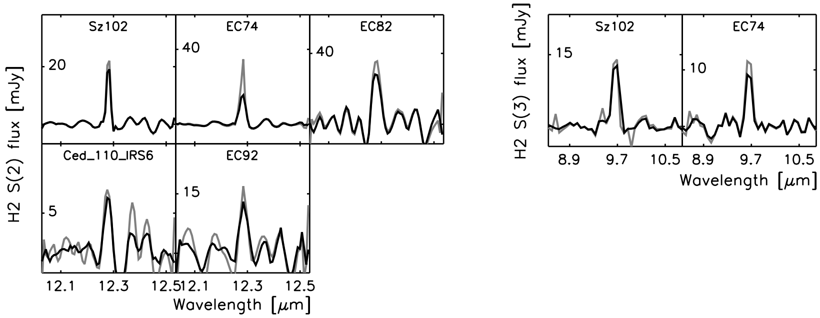

Figure 5.5 Detection of H_2 lines toward the c2d sample of T Tauri stars with disks. Only a few of the 76 sources show clear detections. Plotted in gray is the total observed emission (compact source + extended component) and in black the emission after correction of the estimated extended emission.

upper limits are comparable to the ISO SWS line fluxes. The observed line fluxes and upper limits of the H_2 0-0 S(0), S(1), S(2), and S(3) emission lines are listed in columns $4-7$ of Table 5.2. Figure 5.6 shows the distribution of observed line strengths (solid bars) and upper limits (hatched bars) of H_2 0-0 S(0), S(1), S(2), and S(3).

In the simplest analysis, the H_2 excitation is assumed to be in local thermal equilibrium (LTE) (e.g., Thi et al., 2001) with an ortho-to-para ratio determined by the kinetic temperature of the gas (following Sternberg & Neufeld, 1999). For gas temperatures 100, 150, and ≥200 K, the ortho-to-para ratios are 1.6, 2.5, and 3, respectively. Assuming optically thin emission, the integrated flux of a rotational line $J_u \rightarrow J_l$ for a given temperature $T_{\rm ex}$ is

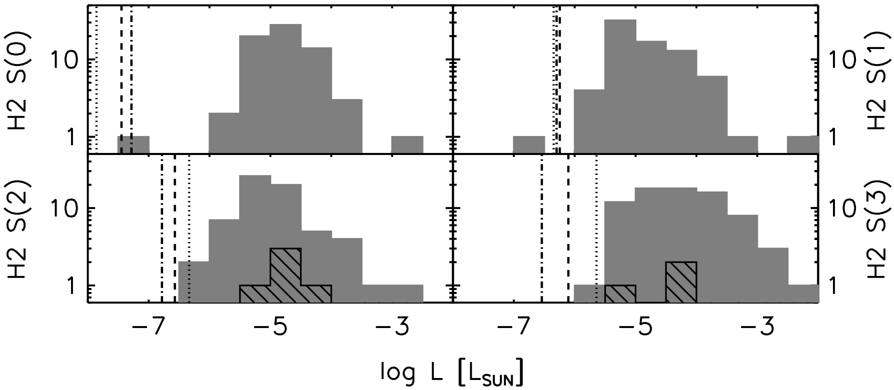

Figure 5.6 Observed line strengths (hatched bars) and upper limits (solid gray bars). The vertical lines present model T Tauri disk line strengths of H_2 S(0), S(1), S(2), and S(3) from Nomura et al. (2007). The models incorporate UV and X-ray heating of the circumstellar disk for three grain size distributions ($a_{\rm max} = 10\mu{\rm m}, 1{\rm mm}$, and $10{\rm cm}$ represented by dotted, dashed, and dashed-dotted lines respectively). For S(0) the line strength increases with increasing maximum grain size, while for S(2) and S(3) the line strength decreases as the maximum grain size increases.

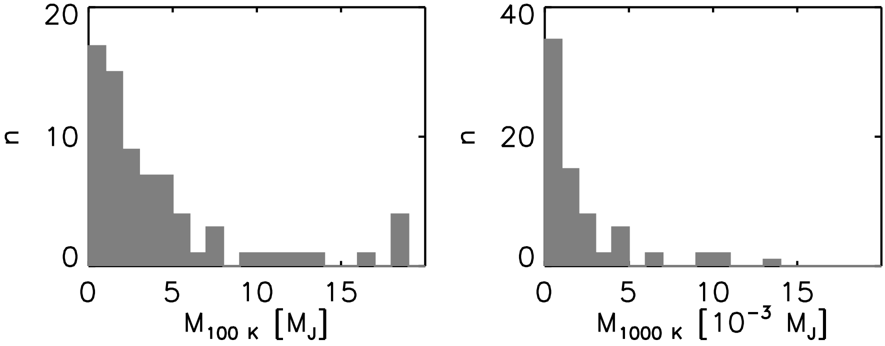

Figure 5.7 Distribution of H_2 mass upper limits derived for 100 and 1000 K gas. The bottom two panels are blow-ups with a smaller binsize of the upper panels.

$$F_{ul} = \frac{hc}{4\pi\lambda} N(\mathrm{H_2}) A_{ul} x_u \Omega \ \mathrm{erg\,s^{-1}\,cm^{-2}}, \tag{5.1}$$

where λ is the wavelength of the transition, $N(\mathrm{H_2})$ the total column density, A_{ul} the spontaneous transition probability, and Ω the source size. For high enough densities ($n \gtrsim 10^3 \mathrm{cm^{-3}}$), the population x_u follows the Boltzmann law

$$x_u = \frac{g_{\mathrm{N}}(2J_u + 1)e^{-E_J/kT_{\mathrm{ex}}}}{Q(T_{\mathrm{ex}})} \tag{5.2}$$

where E_J is the energy of the upper level, g_{N} is the nuclear statistical weight (1 for para and 3 for ortho H_2), and $Q(T_{\mathrm{ex}})$ the partition function for the given excitation temperature T_{ex}.

Using the above equations, excitation temperatures, column densities and H_2 gas masses can be derived from the observed line fluxes and upper limits. If either S(0) or S(1) are detected an upper or lower limit on the temperature of the warm gas is derived, but if neither are detected a temperature of 100 K is assumed for the warm gas. If two or more higher excitation lines (S(2) and higher) are detected a temperature for the hot component is derived, while if no or only one of the higher excitation lines is detected a temperature of 1000 K is assumed. For Sz 102 and EC74 temperatures of $T_{\mathrm{hot}} \sim 700 - 800\,\mathrm{K}$ could be found for the hot component. For all other sources no temperatures could be derived for either component.

The column density averaged over the IRS aperture can be derived from the above equations, given the distance to the source. For all sources in our sample the emitting source size in the disk is smaller than the IRS aperture (§5.3.1) and since this is unknown a typical emitting disk region is assumed. For the warm component a source with a radius $r = 100\,\mathrm{AU}$ is assumed and for the hot component a source with a radius $r = 2\,\mathrm{AU}$. The derived or assumed temperature plus the (upper level) column densities give a total column density, which in turn gives the total H_2 gas mass in Jovian masses, $M = \pi r^2 \times N \times 2m_{\mathrm{H}}/M_{\mathrm{J}}$ with $m_{\mathrm{H}} = 1.674 \cdot 10^{-24}$ gr and $M_{\mathrm{J}} = 1.9 \cdot 10^{30}$ gr.

The derived H_2 parameters for both the warm and hot gas component are listed in Table 5.3. Figure 5.7 shows the distribution of the derived H_2 masses for the assumed temperatures of 100 K and 1000 K, respectively.

5.4.4 Correlations

Figure 5.8 shows the observed line strengths and upper limits of H_2 0-0 S(2), [Ne II], and [Fe I] as functions of the mid-IR luminosities (in Solar luminosities) and the effective temperature. The mid-IR luminosity is also shown as a function of the effective temperature. The mid-IR luminosity is integrated over the 12.8 and 15.5μm continuum points derived in the [Ne II] (12.8μm) and [Ne III] (15.5μm) spectral line fits. The effective temperature is derived from the stellar type (Gray & Corbally, 1994; Baraffe & Chabrier, 1996). In all panels the sources with H_2 0-0 S(2), [Ne II], or [Fe I] detections are

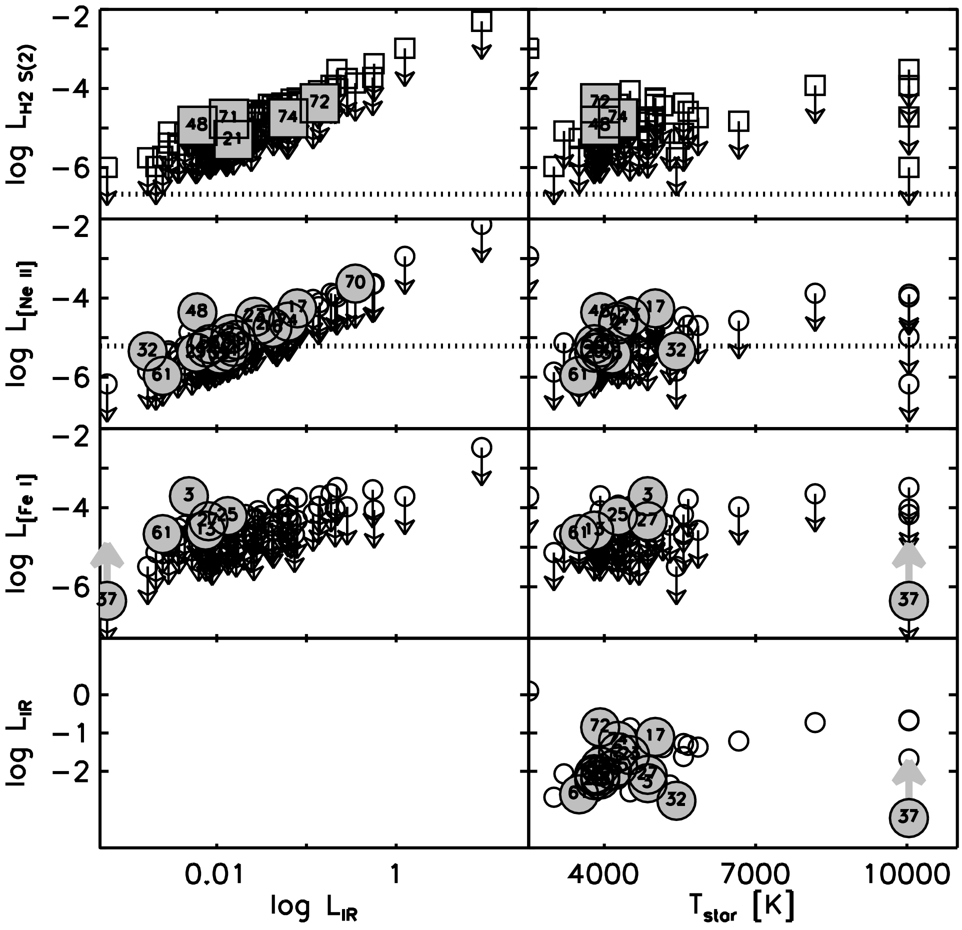

Figure 5.8 Comparison of the observed H_2 S(2) and [Ne II] fluxes in solar luminosities with a few observables. Plotted with the large filled symbols are the line detections, while the small symbols and arrows are all non-detections. Printed in the large filled symbols are the source index numbers. This allows identification of individual sources, in particular the outlier sources such as # 32 – T Cha. The dotted lines in the H_2 and [Ne II] panels show the predicted linefluxes by Nomura et al. (2007) and Glassgold et al. (2007).

plotted with filled large numbered symbols whereas the sources without line detections are plotted with small open gray symbols.

For all sources with detections, both the H_2 0-0 S(2) and [Ne II] line strengths show a positive correlation with the observed mid-IR luminosity. The correlation indicates that there are no low luminosity sources with strong H_2 0-0 S(2) or [Ne II] emission. The upper limits clearly show a S/N selection effect and no conclusion can be drawn about a deviation from the observed correlation to lower H_2 0-0 S(2) or [Ne II] emission fluxes.

The correlation with the effective temperature shows a differentiation between [Ne II] and [Fe I] compared with H_2 0-0 S(2). The [Ne II] and [Fe I] line strengths show a similar correlation with effective temperature as with the mid-IR luminosity, but with more scatter. Also, upper limits are seen below the correlation line for sources with detections. There are a few detected sources deviating from the observed trend, such as the cold disk source T Cha (Brown & et al., 2007) detected in [Ne II] and the Herbig Ae star HD 132947 detected in [Fe I]. T Cha is located at a distance of 66 pc, much closer than the majority of sources in our sample. Sources with a similar [Ne II] line strength as T Cha but at the distances of the nearest star-forming clouds would go undetected at the sensitivity limits of the current sample. For HD 132947 the distance is unknown and the assumed distance of 60 pc is the lower limit from Tycho. The H_2 0-0 S(2) line, although detected for only a small number of sources, differs from [Ne II] and [Fe I] in that all sources are concentrated around one effective temperature. This may be real, but it could also be the result of a S/N selection. More sensitive observations will be required to draw firm conclusions.

The mid-IR luminosity shows a correlation with the effective temperature for most sources. The correlation appears to be tighter for the sources with [Ne II] detections (with the exception of four sources among which T Cha) than for the sources without [Ne II] detections. However, higher sensitivity observations will be required to show the significance of this.

5.5 Discussion

5.5.1 [Ne II]

The most significant outcome of this survey is the detection of [Ne II] emission toward 17 T Tauri stars and one Herbig Ae/Be star, $\gtrsim 20\,\%$ of the sample. [Fe I] is also seen toward 6 sources, $\sim 8\,\%$ of the sample (see §5.4.1 and 5.4.2). Since neon cannot be ionized by photons with energies less than 21.4 eV (and Ne^+ 41.0 eV), the detection of [Ne II] is evidence for the presence of higher energy photons in the circumstellar environment, specifically EUV photons or X-rays originating from either the stellar chromosphere or (accretion) shocks. Alternatively, high-velocity shocks can result in ionized lines.

5.5.1.1 X-ray emission

T Tauri stars are known to be strong emitters of moderately hard X-rays. Feigelson & Lawson (2004) report X-ray luminosities toward young stars in the Chamealeon I north cloud of $L_{\rm X} = 10^{28} - 10^{30}\,{\rm erg\,s^{-1}}$ whereas Telleschi et al. (2006) find X-ray luminosities toward young stars in the Taurus molecular clouds of $L_{\rm X} = 10^{28} - 10^{31}\,{\rm erg\,s^{-1}}$ with a clear stellar mass dependence. A number of sources in our sample have been identified with X-ray sources and have derived X-ray luminosities varying from $L_{\rm X} \sim 4 \times 10^{28} - 10^{31}\,{\rm erg\,s^{-1}}$ (Table 5.4).

Recently Glassgold et al. (2007) modeled the excitation of neon in an X-ray irradiated flaring disk model according to D'Alessio et al. (1999) and predict [Ne II] and [Ne III] line intensities. For a source at 140 pc (the assumed distance in Glassgold et al. (2007)) [Ne II] line fluxes of $(0.6 - 1) \times 10^{-14}$ ${\rm erg\,cm^{-2}\,s^{-1}}$ and [Ne III] line fluxes of $(5 - 6.5) \times 10^{-16}$ ${\rm erg\,cm^{-2}\,s^{-1}}$ are predicted. The predicted [Ne II] line strength of $\sim 4 - 8 \times 10^{-6} L_{\odot}$ falls within the observed range of line strengths (see Table 5.4). The predicted [Ne III] line strength is below the *Spitzer* IRS [Ne III] upper limits. Interestingly the predicted [Ne II] line strength agrees well at 4000 K (the assumed effective temperature in the Glassgold et al. (2007) model) with the trend in the observed line strengths as shown in Figure 5.8.

The Glassgold et al. (2007) model is based on an assumed neon abundance of 10^{-4} and an X-ray luminosity and spectral temperature of $L_{\rm X} = 2 \times 10^{30}\,{\rm erg\,s^{-1}}$ and $kT_{\rm X} = 1\,{\rm keV}$, appropriate for solar-mass pre-main sequence stars observed in Orion (Wolk et al., 2005). Lower mass, older, and accreting stars may have a lower X-ray luminosity (e.g. Feigelson & Lawson, 2004; Preibisch et al., 2005; Telleschi et al., 2006) leading to lower expected line intensities whereas higher X-ray luminosities, higher neon abundances (Drake et al., 2005; Cunha et al., 2006) or the inclusion of H atom collisions (not included in the Glassgold et al. (2007) calculations) may yield higher predicted line intensities. The neon line fluxes also scale with the disk mass surface density and are therefore sensitive to the disk geometry, e.g. flaring or non-flaring disks.

Of the sources with [Ne II] emission about 30 % are identified as X-ray sources. The remaining sources may have escaped detection due to incomplete or sensitivity limited X-ray searches or due to source geometry prohibiting the detection of the X-rays. A more targeted deep X-ray search would be required to confirm a direct relation between observed [Ne II] emission and X-ray luminosities. Overall, variations in X-ray luminosities, age, stellar mass and geometry appear able to cover the two to three orders of magnitude range in the observed [Ne II] line fluxes.

5.5.1.2 EUV radiation

EUV radiation originating from the stellar chromosphere or the accretion shock may be an additional heating component of the disk surface and contribute to the neon excitation. EUV photons are however quickly absorbed by atomic hydrogen in the accretion column (Alexander et al., 2005) and for strong accretors will not reach the disk surface. However, for transitional objects like T Cha the accretion column can become optically thin to EUV photons and some EUV radiation may escape the immediate surroundings of the star and reach the disk surface, potentially contributing to the ionizing radiation at the factor of 2 level. The [Ne II]/[Ne III] ratio is expected to increase with the additional EUV contribution given the high (41.0 eV) ionization potential of $\rm Ne^{+}$. The [Ne III] upper limits do not permit any constraints on this (see Fig. 5.9), however. All [Ne II]/[Ne III] ratios are well below those predicted for X-ray excitation (indicated with the horizontal dashed line). Therefore any enhancement in the [Ne II]/[Ne III] ratio will remain undetected given the sensitivity limits of this sample.

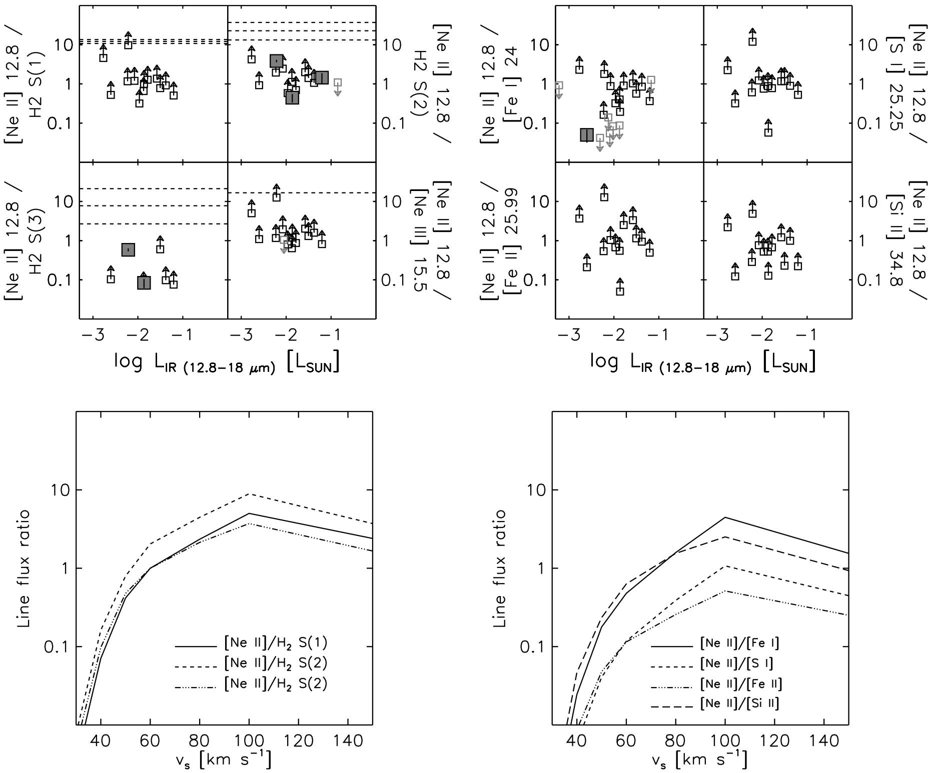

Figure 5.9 Line ratios of [Ne II] w.r.t. other species as functions of mid-IR luminosity. Large filled symbols are used for sources with both [Ne II] and the second line detected. Small open symbols with arrows indicate lower and upper limits of the line ratios. The dashed lines in the left plot show the line ratios for the predictions from the Glassgold et al. (2007); Nomura et al. (2007) models. The lower two plots show the ratios from shock models by Hollenbach & McKee (1989) for different shock velocities.

5.5.1.3 Disk shocks

The presence of strong [Ne II] could also indicate a possible origin of the observed [Ne II] emission induced by shocks in the disk. Hartmann & Raymond (1989) describe shocks resulting from the stellar wind striking the disk surface at an oblique angle. For typical wind velocities of 200 $\mathrm{km\,s^{-1}}$ shock velocities along the disk surface are estimated to be ~30-40 $\mathrm{km\,s^{-1}}$. For such shocks and a medium with a density of $10^5 - 10^6$ $\mathrm{cm^{-3}}$ Hollenbach & McKee (1989) predict [Ne II] line strengths of $\sim 10^{-6} - 10^{-4}$ $\mathrm{erg\,cm^{-2}\,s^{-1}\,sr^{-1}}$. For a 100 AU disk at 100 pc, the upper end of this range implies a [Ne II] line flux of approximately 10^{-14} $\mathrm{erg\,cm^{-2}\,s^{-1}}$, of the same order as observed. However, Hollenbach & McKee (1989) also predict the H_2 0-0 S(1), S(2), and S(3) lines and the [Fe I] 24μm, [S I] 25.25μm, [Fe II] 26μm, and [Si II] 34.8μm spectral lines to be stronger than the [Ne II] line by $1-3$ orders of magnitude for these velocities as illustrated in the lower right plot of Fig. 5.9. The top plots of Fig. 5.9 show the observed ratios and lower limits. For almost all of the line pairs, the ratios are roughly equal to or larger than unity, except for a small number of cases.

To account for line ratios equal to or larger than unity, higher velocity shocks would be required. At high shock velocities ($v \gtrsim 70 \mathrm{km\,s^{-1}}$) and high densities ($\gtrsim 10^5 \mathrm{cm^{-3}}$) the J-shock models presented in Hollenbach & McKee (1989) give [Ne II], [Fe I] 24 μm, [S I] 25.25 μm, [Fe II] 26 μm, and [Si II] 34.8 μm lines all of comparable strength of ∼0.004 $\mathrm{erg\,cm^{-2}\,s^{-1}\,sr^{-1}}$ (see bottom right plot in Figure 5.9). To produce a line flux of $\sim 10^{-14}\,\mathrm{erg\,cm^{-2}\,s^{-1}}$ the shocked emission would have to come from a region of the disk with a radius of ∼10 AU at a distance of 100 pc. Higher velocity shocks may produce the observed line flux ratios and lower limits, but a possible origin for such high velocity shocks is unclear. Another problem lies in the non-detection of the [S I] 25.25μm, the [Fe II] 26μm, and the [Si II] 34.8μm lines. In particular the [S I] line should be detected if high velocity shocks are the origin of the observed line emission: the [S I] line is predicted to be stronger whereas the detection limits for [Fe I] and [S I] are comparable in our data (see Fig. 5.4).

5.5.2 [Fe I] and [S I]

As mentioned in § 5.5.1 the detection of [Fe I] in combination with the non-detection of other atomic lines, in particular [S I] and [Si II], is significant.

Gorti & Hollenbach (2004) modeled the line emission from intermediate aged optically thin disks around G and K stars. For disks with low gas masses (10^{-3} to $10^{-2} M_{\mathrm{J}}$), the [S I] 25.2μm, [Fe II] 26μm, and [Si II] 35.4μm lines are expected to be the strongest mid-infrared emission lines. However as the disk mass increases a larger fraction of the sulfur turns molecular and the [Si II] and [Fe II] emission becomes optically thick. At the same time the [Fe I] lines are predicted to become increasingly stronger and will at some point, around a $0.1 M_{\mathrm{J}}$, dominate over the [S I] emission. Although specific calculations for these optically thick disks are lacking, the six sources (WX Cha, C7-11, LkHα 271, Coku Tau 3, HD 132947, and Haro 1-17) which show strong [Fe I] emission may well have optically thick massive gas-rich disks.

5.5.3 Molecular hydrogen

The second significant result of our survey is the non-detection of the H_2 0-0 S(0) and S(1) lines for 76 T Tauri and Herbig Ae/Be stars. This puts constraints on the mass of warm ($T \sim 100 - 200\,\mathrm{K}$) H_2 gas in the disks around these stars of typically a few M_{Jup} as illustrated in Figure 5.7. Models of disk heating by stellar UV photons show that the gas temperature in the surface layers can be significantly higher than that of the dust down to an optical depth for UV photons of ∼1. The precise temperatures depend on the model details, in particular the presence of PAHs, the grain size, the gas/dust ratio, and the presence of excess UV over that of the stellar photosphere (Jonkheid et al., 2004; Kamp & Dullemond, 2004; Nomura & Millar, 2005; Nomura et al., 2007; Jonkheid et al., 2006, 2007). For interstellar-sized grains (∼0.1 μm), the models readily give surface temperatures of 100 K or more out to at least 100 AU. Even models in which the dust grains have grown and settled to the midplane have warm surface layers as long as some PAHs are still present. The total mass contained in this warm layer is however small, $\sim 1\,\%$ or less of the total disk mass. For the specific 0.07 $M_{\odot}$ disk studied by Jonkheid et al. (2004) the mass at $T > 100\,\mathrm{K}$ is ∼0.7 M_{J}. Thus, for a typical disk mass of 0.01 $\mathrm{M}_{\odot}$, this would be of order 0.1 $\mathrm{M}_{\mathrm{Jup}}$, below our upper limits.

The H_2 line fluxes from a protoplanetary disk representative of that around TW

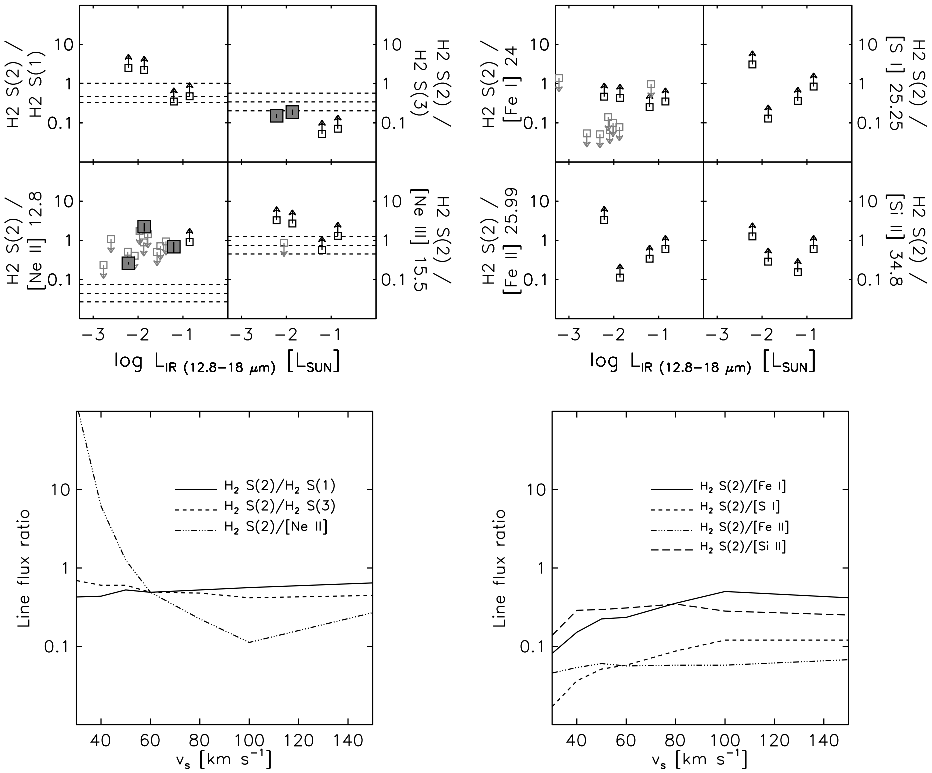

Figure 5.10 Line ratios of H_2 S(2) w.r.t. other species as functions of the mid-IR luminosity. Large filled symbols are used for sources with both H_2 S(2) and the second line detected. Small open symbols with arrows indicate lower and upper limits of the line ratios. The dashed lines In the left plot show the line ratios for the predictions from the Glassgold et al. (2007); Nomura et al. (2007) models. The lower two plots show the ratios from shock models by Hollenbach & McKee (1989) for different shock velocities.

Hya have been modeled by Nomura & Millar (2005). These models include not just thermal excitation but also UV pumping of the H_2 levels. Nomura et al. (2007) include X-ray irradiation and the effect of grain size distributions. For the higher excitation lines the grain size distribution is particularly important with a distribution toward smaller grain sizes producing higher line strengths. This result is consistent with that of Jonkheid et al. (2007), who find lower temperatures in models with grain growth. Figure 5.6 shows the distribution of the observed line strengths with the predicted line strengths for the Nomura et al. (2007) model included for grain size distributions with maximum grain sizes of $a_{\max} = 10\mu\text{m}, 1\text{mm}$, and 10cm. It is seen that the observed upper limits are all consistent with this model, even if excess UV is included. Note, however, that pure rotational H_2 line fluxes are extremely sensitive to the model details: small changes in the heating and cooling processes, as well as the treatment of the H/H_2 transition zone, can result in significant differences in gas temperatures and an order of magnitude variation in predicted line fluxes (see discussion in Li et al., 2002; Roellig et al., 2007). Therefore, comparison of the total mass of warm gas between models and observations is equally relevant.

Toward five sources (~7 % of the sample), H_2 0-0 S(2) and/or S(3) emission is observed, which provides evidence for the presence of a significant hot ($T \gtrsim 500$ K) gas component in the disks. Hot gas ($T \gtrsim 500$ K) is observed toward a number of sources through the H_2 0-0 S(2) line, most convincingly toward Sz 102, EC 82, Ced IRS IRS6, EC 74, and EC 92, For Sz 102 a number of higher transition lines are also seen. The observed H_2 0-0 S(2) line strengths are more than a factor of 10 higher than those predicted in Nomura & Millar (2005); Nomura et al. (2007) (see Fig. 5.6). Given the non-detection of the S(1) line toward the same sources, which is predicted to have a similar strength, this is an indication that these disks have an additional source of emission from hot molecular hydrogen. The upper limits for H_2 0-0 S(2) and S(3) are higher for almost all sources than the Nomura & Millar (2005) predicted values. An additional hot component may therefore be present in these sources as well below our detection limit.

None of the sources with evidence for an additional hot component show evidence for PAH emission (see Geers et al., 2006). Of the five sources with detected H_2 0-0 S(2), four show strong [Ne II] emission, giving support to the idea of a common heating and excitation mechanism through X-rays or EUV. Of the [Ne II] sources two, T Cha and RR Tau, show strong PAH emission. Considering the limitations in observing the PAH emission as described by Geers et al. (2006) we can at this stage draw no conclusions about the relation between the hot H_2 emission, [Ne II] emission, and the importance of PAHs and small grains.

An origin in a high velocity shock as discussed in §5.5.1.3 could produce the enhanced S(2) and S(3) line strengths while keeping the line strengths of S(0) and S(1) reduced. However, as discussed in §5.5.1.3, the main problem with invoking shocks to explain [Ne II] and H_2 is to accommodate both the detections of [Fe I] and the non-detections of [S I] and [Fe II] 26μm. Figure 5.10 shows the observed and model line ratios with respect to H_2, similar those in Fig. 5.9. An origin in an oblique stellar wind shock faces the same problems as discussed for [Ne II] in §5.5.1.3.

5.6 Conclusions

A survey of the mid-infrared gas phase pure rotational lines of molecular hydrogen and a number of atomic fine structure transitions has been carried out toward a significant sample of 76 circumstellar disks with the *Spitzer* IRS. The principal findings include:

- [Ne II] is detected toward $\gtrsim 20$ % of the sources. These present the first detections of [Ne II] toward T Tauri stars. The detections are consistent with disk heating and excitation of [Ne II] through X-rays as presented in Glassgold et al. (2007). Excitation through EUV radiation may contribute. Better constraints on the X-ray luminosities and [Ne III] upper limits are required to distinguish the two contributions.

- [Fe I] is detected toward ~ 8 % of the sources. No other low excitation atomic lines, such as [Fe II], [S I] and [Si II], are detected. This suggests that these sources may possess optically thick disks with gas masses of at least a $0.1 M_\mathrm{J}$.

- No compact H_2 0-0 S(0) and S(1) emission is observed toward any of the sources in our sample, setting limits of a few Jovian masses on the mass of the warm $T_{\rm ex} = 100\,{\rm K}$ gas in the disks. These limits are above model predictions. The H_2 line flux upper limits are also consistent with recent T Tauri disk model predictions by for example Nomura et al. (2007). Earlier tentative ISO detections of H_2 in two Herbig Ae disks are not confirmed.

- Hot ($T \gtrsim 500\,{\rm K}$) H_2 gas has been detected toward $\sim 7\,\%$ of the sources. Given the high upper limits on the rest of the sources, the fraction may be higher. The detection of the hot gas suggests the presence of an additional source of hot H_2 emission not included in the most recent disk models (e.g. Nomura et al., 2007).

- Of the five sources with hot H_2 emission four show [Ne II] emission suggesting a possible common heating and excitation mechanism through X-rays or EUV.

- Lower limits of the line flux ratios of [Ne II] with H_2 and [Ne III] are consistent with recent T Tauri disk models presented in Glassgold et al. (2007); Nomura et al. (2007).

- An origin of the enhanced H_2 emission in oblique shocks due to winds interacting with the disk surface is not consistent with the non-detection of atomic lines, in particular the non-detections of [S I] and [Fe II] 26μm.

The bright [Ne II] lines detected at 12.8 μm are excellent targets for follow-up observations with high dispersion echelle spectrometers on 8-10m class telescopes (TEXES, VISIR). The measured spatial profiles and line shapes would provide exacting tests of the X-ray mediated disk emission proposed here and could definitely rule out any high-velocity shock mechanism.

Acknowledgements

The authors would like to thank Jes Jørgensen for making the *Spitzer* IRAC mosaics, and Hideko Nomura for communicating her latest disk model results. Astrochemistry in Leiden is supported by a NWO Spinoza grant and a NOVA grant. Support for this work, part of the *Spitzer* Legacy Science Program, was provided by NASA through contracts 1224608, 1230779, and 1256316 issued by the Jet Propulsion Laboratory, California Institute of Technology, under NASA contract 1407. We thank the Lorentz Center in Leiden for hosting several meetings that contributed to this paper.

Table 5.1. Source list

#	Source [1]	RA [2]	Dec [3]	AOR [4]	tint [s] (SL/SH/LH)/ndith. [5]	Class [6]	D^{a} [pc] [7]	Age [Myr] [8]	Spectral type [9]
1	RNO 15	$3^{h}\,27^{m}\,47^{s}.7$	$30^{\circ}\,12'\,04''.3$	5633280	(14*1/31*2/60*1)*2	TTs	250	-	-
2	Lk Hα 270	$3^{h}\,29^{m}\,17^{s}.7$	$31^{\circ}\,22'\,45''.1$	5634048	(14*2/31*2/60*2)*2	TTs	250	0.014	K2.5-K7
3	Lk Hα 271	$3^{h}\,29^{m}\,21^{s}.9$	$31^{\circ}\,15'\,36''.4$	11827968	(14*2/121*2/60*2)*2	TTs	250	-	K3-K5
4	Lk Hα 326	$3^{h}\,30^{m}\,44^{s}.0$	$30^{\circ}\,32'\,46''.7$	5634304	(14*2/31*4/60*1)*2	TTs	250	0.28	G-M0
5	Lk Hα 327	$3^{h}\,33^{m}\,30^{s}.4$	$31^{\circ}\,10'\,50''.5$	5634560	(14*1/6*2/14*2)*2	TTs	250	0.70-1.4	A9-K2
6	Lk Hα 330	$3^{h}\,45^{m}\,48^{s}.3$	$32^{\circ}\,24'\,11''.9$	5634816	(14*1/31*1/60*1)*2	CTTs	250	5.72	G3
7	IRAS 03446+3254	$3^{h}\,47^{m}\,47^{s}.1$	$33^{\circ}\,04'\,03''.4$	5635072	(14*1/121*2/60*1)*2	TTs	250	-	-
8	LkCa 8	$4^{h}\,24^{m}\,57^{s}.1$	$27^{\circ}\,11'\,56''.4$	9832960	(–/31*8/60*2)*2	CTTs	140	-	M0-M0Ve
9	IQ Tau	$4^{h}\,29^{m}\,51^{s}.6$	$26^{\circ}\,06'\,45''.0$	9832704	(–/31*2/60*2)*2	WTTs	140	1.2	M0-M0.5
10	FX Tau	$4^{h}\,30^{m}\,29^{s}.6$	$24^{\circ}\,26'\,45''.2$	9832448	(–/31*2/60*2)*2	C+WTTs	140	-	M1-M4
11	V710 Tau	$4^{h}\,31^{m}\,57^{s}.8$	$18^{\circ}\,21'\,36''.4$	5636608	(–/121*2/60*4)*2	C+WTTs	140	-	M0.5-M1-M2-M3
12	DN Tau	$4^{h}\,35^{m}\,27^{s}.4$	$24^{\circ}\,14'\,58''.9$	9831936	(–/31*4/60*2)*2	CTTs	140	-	M0
13	CoKu Tau 3	$4^{h}\,35^{m}\,40^{s}.9$	$24^{\circ}\,11'\,08''.5$	9831936	(–/31*4/60*2)*2	CTTs	140	-	M1
14	CoKu Tau 4	$4^{h}\,41^{m}\,16^{s}.8$	$28^{\circ}\,40'\,00''.5$	5637888	(–/31*2/60*4)*2	CTTs	140	1.2-1.6	M1.5
15	BF Ori	$5^{h}\,37^{m}\,13^{s}.3$	$-6^{\circ}\,35'\,00''.6$	5638144	(14*1/31*1/60*1)*2	HAeBe	400	2.0	A5-F6
16	RR Tau	$5^{h}\,39^{m}\,30^{s}.5$	$26^{\circ}\,22'\,27''.1$	5638400	(14*1/31*1/60*1)*2	HAeBe	160	0.6	A5-B8
17	IRAS 08267-3336	$8^{h}\,28^{m}\,40^{s}.7$	$-33^{\circ}\,46'\,22''.4$	5639168	(14*1/31*2/60*1)*2	TTs	400?	1.96	K2-K2.5-K3
18	SX Cha	$10^{h}\,55^{m}\,59^{s}.7$	$-77^{\circ}\,24'\,40''.0$	5639424	(–/121*1/60*2)*2	TTs	178	1.15-1-4	M0.5
19	SY Cha	$10^{h}\,56^{m}\,30^{s}.5$	$-77^{\circ}\,11'\,39''.5$	5639424	(–/121*1/60*2)*2	TTs	178	1.35-2-5	M0
20	TW Cha	$10^{h}\,59^{m}\,01^{s}.1$	$-77^{\circ}\,22'\,40''.8$	5639680	(–/121*2/60*2)*2	TTs	178	16.82-20	K0-M0
21	Ced 110 IRS6	$11^{h}\,07^{m}\,09^{s}.2$	$-77^{\circ}\,23'\,04''.2$	5639680	(–/121*2/60*2)*2	1	178	-	-
22	B35	$11^{h}\,07^{m}\,21^{s}.5$	$-77^{\circ}\,22'\,11''.7$	5639680	(–/121*2/60*2)*2	TTs	178	0.1	M2
23	VW Cha	$11^{h}\,08^{m}\,01^{s}.5$	$-77^{\circ}\,42'\,28''.8$	5639680	(–/121*2/60*2)*2	CTTs	178	2.39-0.2-1.0	K2-K5-K5K7
24	VZ Cha	$11^{h}\,09^{m}\,23^{s}.8$	$-76^{\circ}\,23'\,20''.8$	5640448	(–/121*2/60*2)*2	TTs	178	5.71-4-10	K6-K7
25	WX Cha	$11^{h}\,09^{m}\,58^{s}.8$	$-77^{\circ}\,37'\,08''.8$	5640192	(–/121*1/60*2)*2	TTs	178	0.79-1-5	K7-M0
26	ISO-Cha237	$11^{h}\,10^{m}\,11^{s}.4$	$-76^{\circ}\,35'\,29''.0$	5640448	(–/121*2/60*2)*2	TTs	178	-	M0
27	C7-11	$11^{h}\,10^{m}\,38^{s}.0$	$-77^{\circ}\,32'\,39''.9$	5640192	(–/121*1/60*2)*2	TTs	178	0.2-1	K3
28	HM 27	$11^{h}\,10^{m}\,49^{s}.6$	$-77^{\circ}\,17'\,51''.7$	5640192	(–/121*1/60*2)*2	TTs	178	2.38-30-40	K7
29	XX Cha	$11^{h}\,11^{m}\,39^{s}.7$	$-76^{\circ}\,20'\,15''.0$	5640448	(–/121*2/60*2)*2	TTs	178	1.87-2-40	M1-M2
30	HD 98922	$11^{h}\,22^{m}\,31^{s}.7$	$-53^{\circ}\,22'\,11''.3$	5640704	(–/6*1/14*1)*2	HAeBe	¿ 540	-	B9

Table 5.1—Continued

#	Source [1]	RA [2]	Dec [3]	AOR [4]	tint [s] (SL/SH/LH)/ndith. [5]	Class [6]	D[a] [pc] [7]	Age [Myr] [8]	Spectral type [9]
31	HD 101412	$11^{h}\,39^{m}\,44^{s}.5$	$-60^{\circ}\,10'\,27''.8$	5640960	(14*1/31*1/60*1)*2	HAeBe	160	-	B9.5V
32	T Cha	$11^{h}\,57^{m}\,13^{s}.5$	$-79^{\circ}\,21'\,31''.3$	5641216	(–/31*2/60*1)*2	TTs	66	4.14-¿12.5	G2-G8-K0
33	IRAS 12535-7623	$12^{h}\,57^{m}\,11^{s}.8$	$-76^{\circ}\,40'\,11''.6$	11827456	(–/121*1/60*2)*2	TTs	178	0.19	M0
34	Sz50	$13^{h}\,00^{m}\,55^{s}.4$	$-77^{\circ}\,10'\,22''.1$	11827456	(–/121*1/60*2)*2	TTs	178	1.74	K7-M3
35	ISO-ChaII 54	$13^{h}\,00^{m}\,59^{s}.2$	$-77^{\circ}\,14'\,02''.8$	15735040	(14*2/31*4/–)*2	BD	178	-	-
36	DL Cha	$13^{h}\,06^{m}\,08^{s}.4$	$-77^{\circ}\,06'\,27''.4$	5642240	(–/6*2/6*5)*2	TTs	178	-	III-M6
37	HD 132947	$15^{h}\,04^{m}\,56^{s}.0$	$-63^{\circ}\,07'\,52''.7$	5643008	(14*1/31*2/241*2)*2	HAeBe	¿60	-	A0
38	HD 135344	$15^{h}\,15^{m}\,48^{s}.4$	$-37^{\circ}\,09'\,15''.8$	5657088	(–/121*1/60*2)*2	HAeBe	140	17	A0-F4
39	HT Lup	$15^{h}\,45^{m}\,12^{s}.9$	$-34^{\circ}\,17'\,30''.5$	5643264	(14*1/31*1/60*1)*2	TTs	145	2.29-0.4-0.8	K2
40	HT Lup	$15^{h}\,45^{m}\,12^{s}.9$	$-34^{\circ}\,17'\,30''.5$	9829120	(14*2/31*2/60*2)*1	TTs	145	2.29-0.4-0.8	K2
41	GW Lup	$15^{h}\,46^{m}\,44^{s}.7$	$-34^{\circ}\,30'\,35''.3$	5643520	(14*1/121*2/60*4)*2	TTs	100	3.40-1.3-3.2	M2-M4
42	Sz73	$15^{h}\,47^{m}\,57^{s}.0$	$-35^{\circ}\,14'\,35''.2$	5644032	(14*1/31*1/60*1)*2	TTs	100	3.24-2.6-5.4	K2-K5-M0-M
43	GQ Lup	$15^{h}\,49^{m}\,12^{s}.1$	$-35^{\circ}\,39'\,05''.0$	5644032	(14*1/31*1/60*1)*2	TTs	100	0.96-0.1-0.6	K7-M0
44	IM Lup	$15^{h}\,56^{m}\,09^{s}.2$	$-37^{\circ}\,56'\,06''.4$	5644800	(14*1/31*2/60*1)*2	TTs	140	1.51-0.1-0.6	M0
45	RU Lup	$15^{h}\,56^{m}\,42^{s}.3$	$-37^{\circ}\,49'\,15''.6$	5644800	(14*1/31*2/60*1)*2	CTTs	140	0.82-0.1-0.5	K3-K7-M0
46	RY Lup	$15^{h}\,59^{m}\,28^{s}.4$	$-40^{\circ}\,21'\,51''.1$	5644544	(14*1/31*1/60*1)*2	TTs	150	2.67-1.6-3.2	K0-K4
47	EX Lup	$16^{h}\,03^{m}\,05^{s}.5$	$-40^{\circ}\,18'\,24''.8$	5645056	(14*1/31*1/60*1)*2	TTs	150	5.62-1.4-3.0	M0
48	Sz102	$16^{h}\,08^{m}\,29^{s}.7$	$-39^{\circ}\,03'\,11''.2$	9407488	(14*1/121*2/60*1)*2	TTs	200	-	M0
49	AS 205	$16^{h}\,11^{m}\,31^{s}.3$	$-18^{\circ}\,38'\,26''.2$	5646080	(6*2/6*2/14*2)*2	TTs	120	0.43-0.1	K5
50	Haro 1-1	$16^{h}\,21^{m}\,34^{s}.7$	$-26^{\circ}\,12'\,27''.0$	9833472	(14*1/31*4/60*1)*2	CTTs	125	13.1	K5-K7
51	Haro 1-4	$16^{h}\,25^{m}\,10^{s}.5$	$-23^{\circ}\,19'\,14''.5$	9833216	(–/31*2/60*1)*2	TTs	125	0.80	7-K4-K6
52	DoAr 24E	$16^{h}\,26^{m}\,23^{s}.4$	$-24^{\circ}\,21'\,00''.0$	5647616	(–/31*1/14*2)*2	TTs	125	2.46-1.5	K0-K1
53	SR 21	$16^{h}\,27^{m}\,10^{s}.3$	$-24^{\circ}\,19'\,12''.4$	5647616	(–/31*1/14*2)*2	TTs	125	3.04-1	F4-G1,G2.5
54	IRS51	$16^{h}\,27^{m}\,39^{s}.8$	$-24^{\circ}\,43'\,15''.2$	9829888	(–/31*2/14*2)*2	2	125	0.79	G5-K7
55	SR 9	$16^{h}\,27^{m}\,40^{s}.3$	$-24^{\circ}\,22'\,04''.1$	12027392	(–/31*1/60*2)*2	TTs	125	0.83	K5,M2-K8
56	V853Oph	$16^{h}\,28^{m}\,45^{s}.3$	$-24^{\circ}\,28'\,18''.8$	12408576	(–/31*4/60*4)*2	TTs	125	0.78	M1.5
57	ROX42C	$16^{h}\,31^{m}\,15^{s}.7$	$-24^{\circ}\,34'\,01''.9$	6369792	(–/31*2/60*1)*2	TTs	125	3.7-(Fi)	K4-K5-K6
58	ROX43A	$16^{h}\,31^{m}\,20^{s}.1$	$-24^{\circ}\,30'\,05''.0$	15914496	(–/31*1/60*2)*2	TTs	125	12.2	G0
59	IRS60	$16^{h}\,31^{m}\,30^{s}.9$	$-24^{\circ}\,24'\,39''.6$	6370048	(–/31*1/60*1)*2	-	125	-	-
60	Haro 1-16	$16^{h}\,31^{m}\,33^{s}.5$	$-24^{\circ}\,27'\,37''.1$	12664064	(–/31*1/60*1)*2	TTs	125	1.92-0.5	K2-K3

Table 5.1—Continued

#	Source [1]	RA [2]	Dec [3]	AOR [4]	tint [s] (SL/SH/LH)/ndith. [5]	Class [6]	D[a] [pc] [7]	Age [Myr] [8]	Spectral type [9]
61	Haro 1-17	$16^{h}\,32^{m}\,21^{s}.9$	$-24^{\circ}\,42'\,14''.8$	11827712	(60*1/121*4/60*4)*2	TTs	125	-	M2.5
62	RNO 90	$16^{h}\,34^{m}\,09^{s}.2$	$-15^{\circ}\,48'\,16''.9$	5650432	(14*1/31*1/14*2)*2	TTs	140	6	G5
63	Wa Oph 6	$16^{h}\,48^{m}\,45^{s}.6$	$-14^{\circ}\,16'\,35''.8$	5650688	(14*1/31*1/60*1)*2	2	140	0.85	K7
64	V1121 Oph	$16^{h}\,49^{m}\,15^{s}.3$	$-14^{\circ}\,22'\,08''.8$	5650688	(14*1/31*1/60*1)*2	CTTs	125	0.53	K5
65	HD 163296	$17^{h}\,56^{m}\,21^{s}.3$	$-21^{\circ}\,57'\,22''.0$	5650944	(–/6*2/14*2)*2	HAeBe	122	4-6	A0-A2
66	HD 163296	$17^{h}\,56^{m}\,21^{s}.3$	$-21^{\circ}\,57'\,22''.0$	9830144	(–/6*4/14*4)*1	HAeBe	122	4-6	A0-A2
67	VV Ser	$18^{h}\,28^{m}\,47^{s}.9$	$0^{\circ}\,08'\,39''.8$	5651200	(6*2/31*1/60*1)*2	HAeBe	260	0.6	A3-B1
68	SSTc2d J182900.9+02931	$18^{h}\,29^{m}\,00^{s}.9$	$0^{\circ}\,29'\,31''.6$	13210112	(14*1/31*2/–)*2	-	260	-	-
69	SSTc2d J182909.8+03446	$18^{h}\,29^{m}\,09^{s}.8$	$0^{\circ}\,34'\,45''.8$	13210624	(14*1/31*1/–)*2	-	260	-	-
70	SSTc2d J182928.2+02257	$18^{h}\,29^{m}\,28^{s}.2$	$-0^{\circ}\,22'\,57''.4$	13210368	(14*1/31*2/–)*2	-	260	-	-
71	EC74	$18^{h}\,29^{m}\,55^{s}.7$	$1^{\circ}\,14'\,31''.6$	9407232	(14*1/121*1/60*2)*2	2	260	-	-
72	EC82	$18^{h}\,29^{m}\,56^{s}.9$	$1^{\circ}\,14'\,46''.7$	9407232	(14*1/121*1/60*2)*2	TTs	260	-	M0
73	EC90	$18^{h}\,29^{m}\,57^{s}.7$	$1^{\circ}\,14'\,06''.0$	9828352	(6*2/31*1/14*1)*2	TTs	260	-	-
74	EC92	$18^{h}\,29^{m}\,57^{s}.9$	$1^{\circ}\,12'\,51''.5$	9407232	(14*1/121*1/60*2)*2	TTs	260	-	K7-M2
75	CK4	$18^{h}\,29^{m}\,58^{s}.2$	$1^{\circ}\,15'\,21''.6$	9407232	(14*1/121*1/60*2)*2	TTs	260	6.81	K3
76	Lk Hα 348	$18^{h}\,34^{m}\,12^{s}.6$	$-0^{\circ}\,26'\,21''.8$	9831424	(6*2/6*2/14*2)*2	-	260	-	-

[a] Assumed cloud distances; Chamaeleon (178 pc Whittet et al., 1997) Lupus I, IV (150 pc) and Lupus III (200 pc) Comeron in prep., Ophiuchus (125 pc de Geus et al., 1989), Perseus (250 pc, see discussion in Enoch, Young, Glenn, Evans, Golwala, Sargent, Harvey, Aguirre, Goldin, Haig, Huard, Lange, Laurent, Maloney, Mauskopf, Rossinot, & Sayers, 2006), Taurus-Auriga (160 pc Kenyon et al., 1994), Serpens (260 pc Straizys, Cernis, & Bartasiute, 1996), except for T Cha, HD 98922, & HD 163296 (van den Ancker et al., 1998), BF Ori, (Parenago, 1954), HD 101412 & HD 135344 (de Zeeuw et al., 1999), & HD 132947 (minimum Tycho distance)

A literature reference list is included in the source table of the published ApJ paper.

Table 5.2. Observed linefluxes and 1σ uncertainties ($10^{-16}\mathrm{erg\,cm^{-2}\,s^{-1}}$)

# [1]	Source [2]	Dis. [pc] [3]	H_2 S(0) [4]	H_2 S(1) [5]	H_2 S(2) [6]	H_2 S(3) [7]	[Ne II] [8]	[Ne III] [9]	[Fe I] [10]	[Fe II] 18 [11]	[Fe II] 25 [12]	[S I] [13]	[Si II] [14]
1	RNO 15	250	– (63)	– (93)	– (28)	– (640)	– (95)	– (74)	– (74)	– (88)	– (50)	– (50)	– (41)
2	Lk Hα 270	250	– (37)	– (47)	– (26)	– (61)	110 (36)	– (28)	– (65)	– (37)	– (32)	– (31)	– (160)
3	Lk Hα 271	250	– (48)	– (11)	– (17)	– (42)	– (14)	– (8)	1000 (140)	– (16)	– (18)	– (25)	– (200)
4	Lk Hα 326	250	– (36)	– (33)	– (23)	– (150)	– (26)	– (28)	– (86)	– (26)	– (15)	– (38)	– (120)
5	Lk Hα 327	250	– (89)	– (90)	– (55)	– (320)	– (72)	– (57)	170 (49)	– (90)	– (41)	– (54)	– (45)
6	Lk Hα 330	250	– (140)	– (62)	– (27)	– (210)	– (21)	– (34)	– (170)	– (42)	– (110)	– (110)	– (89)
7	IRAS 03446+3254	250	– (89)	– (12)	– (9)	– (73)	64 (9)	– (14)	– (87)	– (18)	– (40)	– (49)	– (110)
8	LkCa 8	140	– (20)	– (17)	– (12)		– (13)	– (12)	– (64)	– (16)	– (31)	– (28)	– (120)
9	IQ Tau	140	– (45)	– (27)	– (25)		– (30)	86 (26)	– (59)	– (22)	– (19)	– (38)	– (150)
10	FX Tau	140	– (43)	– (34)	– (40)		– (22)	– (24)	– (98)	– (29)	– (30)	– (16)	– (140)
11	V710 Tau	140	– (63)	– (16)	– (12)		– (8)	– (12)	– (100)	– (15)	– (34)	– (33)	– (73)
12	DN Tau	140	– (33)	– (25)	– (27)		– (18)	– (17)	– (73)	– (18)	– (26)	– (38)	– (86)
13	CoKu Tau 3	140	– (26)	– (27)	– (20)		– (20)	– (16)	430 (69)	– (28)	– (31)	– (15)	– (61)
14	CoKu Tau 4	140	– (60)	– (34)	– (26)		– (13)	– (17)	– (110)	– (37)	– (37)	– (39)	– (100)
15	BF Ori	400	– (120)	– (58)	– (48)	– (1400)	– (53)	– (43)	– (90)	– (62)	– (33)	– (230)	– (51)
16	RR Tau	160	– (65)	– (80)	– (69)	– (750)	220 (72)	– (46)	– (86)	– (52)	– (78)	– (82)	– (74)
17	IRAS 08267-3336	400?	– (43)	– (29)	– (23)	– (85)	110 (25)	– (23)	– (72)	– (32)	– (24)	– (26)	– (32)
18	SX Cha	178	– (61)	– (28)	– (20)		– (27)	– (20)	– (49)	– (29)	– (25)	– (32)	– (38)
19	SY Cha	178	– (45)	– (17)	– (14)		– (13)	– (11)	– (64)	– (23)	– (38)	– (22)	– (58)
20	TW Cha	178	– (62)	– (24)	– (15)		– (12)	– (19)	– (73)	– (18)	– (28)	– (39)	– (46)
21	Ced 110 IRS6	178	– (73)	– (38)	50 (12)		59 (17)	– (22)	– (59)	– (36)	– (51)	– (49)	– (48)
22	B35	178	– (52)	– (14)	– (11)		– (6)	– (15)	– (48)	– (13)	– (16)	– (16)	– (60)
23	VW Cha	178	– (84)	– (83)	– (57)		340 (40)	– (56)	– (110)	– (61)	– (34)	– (97)	– (93)
24	VZ Cha	178	– (64)	– (23)	– (34)		– (28)	– (36)	– (58)	– (24)	– (38)	– (29)	– (38)
25	WX Cha	178	– (29)	– (29)	– (16)		– (18)	– (26)	620 (49)	– (27)	– (61)	– (24)	– (39)
26	ISO-Cha237	178	– (43)	– (23)	– (11)		– (23)	– (18)	– (94)	– (27)	– (36)	– (40)	– (45)
27	C7-11	178	– (28)	– (11)	– (10)		– (8)	– (12)	460 (48)	– (15)	– (36)	– (20)	– (38)
28	HM 27	178	– (38)	– (21)	– (12)		– (10)	– (23)	360 (55)	– (22)	– (50)	– (20)	– (39)
29	XX Cha	178	– (36)	– (12)	– (7)		42 (9)	– (12)	– (86)	– (14)	– (26)	– (23)	– (49)
30	HD 98922	¿ 540	– (510)	– (1200)	– (1100)		– (1600)	– (750)	– (730)	– (1100)	– (380)	– (500)	– (180)
31	HD 101412	160	– (83)	– (120)	– (110)	– (930)	– (140)	– (74)	– (120)	– (120)	– (36)	– (77)	– (66)
32	T Cha	66	– (47)	– (24)	– (26)		330 (21)	– (22)	– (48)	– (33)	– (30)	– (49)	– (50)
33	IRAS 12535-7623	178	– (63)	– (21)	– (12)		– (20)	– (13)	– (66)	– (19)	– (30)	– (25)	– (45)
34	Sz50	178	– (48)	– (19)	– (17)		– (15)	– (13)	– (43)	– (15)	– (47)	– (21)	– (80)
35	ISO-ChaII 54	178		– (15)	– (17)	– (130)	– (13)	– (11)		– (24)			
36	DL Cha	178	– (400)	– (1000)	– (2100)		– (2300)	– (1500)	– (390)	– (1100)	– (430)	– (360)	– (140)
37	HD 132947	¿ 60	– (2)	– (7)	– (18)	– (180)	– (12)	– (20)	39 (6)	– (29)	– (5)	– (4)	– (18)
38	HD 135344	140	– (150)	– (68)	– (62)		– (34)	– (45)	– (220)	– (67)	– (150)	– (140)	– (160)

Table 5.2—Continued

# [1]	Source [2]	Dis. [pc] [3]	H_2 S(0) [4]	H_2 S(1) [5]	H_2 S(2) [6]	H_2 S(3) [7]	[Ne II] [8]	[Ne III] [9]	[Fe I] [10]	[Fe II] 18 [11]	[Fe II] 25 [12]	[S I] [13]	[Si II] [14]
39	HT Lup	145	– (120)	– (110)	– (48)	– (760)	– (110)	– (75)	– (160)	– (81)	– (63)	– (100)	– (74)
40	HT Lup	145	– (200)	– (250)	– (120)	– (1100)	– (170)	– (200)	– (210)	– (260)	– (130)	– (170)	– (110)
41	GW Lup	100	– (49)	– (13)	– (6)	– (65)	– (8)	– (16)	– (47)	– (28)	– (42)	– (11)	– (29)
42	Sz73	100	– (46)	– (47)	– (41)	– (150)	180 (32)	– (43)	– (81)	– (44)	– (41)	– (44)	– (50)
43	GQ Lup	100	– (27)	– (43)	– (36)	– (230)	– (30)	– (45)	– (81)	– (57)	– (45)	– (31)	– (84)
44	IM Lup	140	– (52)	– (36)	– (21)	– (330)	71 (22)	– (37)	– (59)	– (34)	– (43)	– (27)	– (45)
45	RU Lup	140	– (150)	– (150)	– (130)	– (830)	– (100)	– (130)	– (140)	– (130)	– (110)	– (160)	– (72)
46	RY Lup	150	– (100)	– (54)	– (40)	– (490)	– (38)	– (42)	– (100)	– (120)	– (78)	– (81)	– (90)
47	EX Lup	150	– (58)	– (39)	– (35)	– (230)	– (23)	– (54)	– (94)	– (46)	– (52)	– (43)	– (110)
48	Sz102	200	– (34)	– (12)	91 (6)	600 (52)	350 (7)	– (9)	– (65)	67 (15)	– (9)	– (9)	– (24)
49	AS 205	120	– (280)	– (540)	– (390)	– (3700)	– (270)	– (450)	– (480)	– (450)	– (280)	– (310)	– (160)
50	Haro 1-1	125	– (26)	– (26)	– (17)	– (55)	– (19)	– (15)	– (43)	– (22)	– (23)	– (39)	– (52)
51	Haro 1-4	125	– (26)	– (35)	– (36)		– (25)	– (31)	– (81)	– (49)	– (38)	– (44)	– (120)
52	DoAr 24E	125	– (110)	– (140)	– (150)		– (120)	– (150)	– (170)	– (240)	– (120)	– (77)	– (98)
53	SR 21	125	– (320)	– (340)	– (61)		– (110)	– (180)	– (430)	– (410)	– (450)	– (460)	– (260)
54	IRS51	125	– (160)	– (65)	– (30)		– (47)	– (36)	– (86)	– (61)	– (110)	– (65)	– (91)
55	SR 9	125	– (53)	– (81)	– (44)		77 (24)	– (32)	– (80)	– (81)	– (38)	– (34)	– (49)
56	V853Oph	125	– (42)	– (39)	– (19)		140 (25)	– (24)	– (53)	– (31)	– (45)	– (38)	– (61)
57	ROX42C	125	– (48)	– (46)	– (23)		– (23)	– (41)	– (41)	– (39)	– (18)	– (29)	– (73)
58	ROX43A	125	– (73)	– (150)	– (75)		– (83)	– (92)	– (110)	– (120)	– (49)	– (110)	– (67)
59	IRS60	125	– (33)	– (47)	– (86)		180 (52)	– (69)	– (66)	– (50)	– (24)	– (77)	– (89)
60	Haro 1-16	125	– (48)	– (82)	– (35)		– (38)	– (51)	– (120)	– (56)	– (25)	– (72)	– (81)
61	Haro 1-17	125	– (57)	– (14)	– (7)	– (71)	22 (6)	– (6)	440 (82)	– (21)	– (35)	– (23)	– (60)
62	RNO 90	140	– (160)	– (240)	– (140)	– (870)	– (110)	– (170)	– (220)	– (180)	– (130)	– (230)	– (99)
63	Wa Oph 6	140	– (37)	– (100)	– (67)	– (470)	– (61)	– (68)	– (43)	– (47)	– (17)	– (30)	– (21)
64	V1121 Oph	125	– (56)	– (260)	– (120)	– (2200)	– (200)	– (140)	– (87)	– (280)	– (59)	– (93)	– (52)
65	HD 163296	122	– (400)	– (910)	– (510)		– (540)	– (370)	– (400)	– (800)	– (270)	– (400)	– (170)
66	HD 163296	122	– (650)	– (1400)	– (1300)		– (460)	– (1300)	– (1400)	– (1300)	– (220)	– (430)	– (350)
67	VV Ser	260	– (94)	– (250)	– (170)	– (2600)	– (140)	– (160)	– (100)	– (130)	– (73)	– (89)	– (83)
68	SSTc2d J182900.9	260		– (36)	– (30)	– (170)	– (16)	– (35)		– (52)			
69	SSTc2d J182909.8	260		– (66)	– (44)	– (340)	– (53)	– (35)		– (88)			
70	SSTc2d J182928.2	260		– (170)	– (130)	– (1500)	1100 (150)	– (160)		– (250)			
71	EC74	260	– (78)	– (12)	81 (7)	430 (55)	36 (8)	– (10)	– (62)	– (17)	– (240)	– (210)	– (94)
72	EC82	260	– (90)	– (140)	200 (38)	– (940)	– (73)	– (51)	– (190)	– (130)	– (110)	– (79)	– (110)
73	EC90	260	– (230)	– (570)	– (180)	– (6900)	– (210)	– (320)	– (270)	– (890)	– (290)	– (280)	– (210)
74	EC92	260	– (110)	– (79)	83 (20)	– (530)	120 (22)	– (49)	– (110)	– (67)	– (81)	– (76)	– (180)
75	CK4	260	– (34)	– (29)	– (18)	– (81)	– (15)	– (25)	– (47)	– (26)	– (19)	– (22)	– (62)
76	Lk Hα 348	260	– (55)	– (190)	– (400)	– (3100)	– (220)	– (290)	– (83)	– (760)	– (32)	– (42)	– (27)

Table 5.3. Diagnostic parameters of the disk gas contents.

#[a]	Source	T_{warm}[b] [K]	N_{warm}[b] ($r = 100$ AU)[c] [$10^{22}\mathrm{cm}^{-2}$]	M_{warm}[b] [$\mathrm{M_J}$]	T_{hot}[b] [K]	N_{hot} ($r = 2$ AU)[c] [$10^{22}\mathrm{cm}^{-2}$]	M_{hot} [$10^{-3}\mathrm{M_J}$]
1	RNO 15		< 60	< 7.4		< 82	< 4.0
2	Lk Hα 270		< 35	< 4.4		< 27	< 1.4
3	Lk Hα 271		< 28	< 3.5		< 25	< 1.3
4	Lk Hα 326		< 34	< 4.2		< 67	< 3.3
5	Lk Hα 327		< 85	< 10.6		< 137	< 6.9
6	Lk Hα 330		< 130	< 16.7		< 95	< 4.7
7	IRAS 03446+3254		< 30	< 3.8		< 62	< 3.1
8	LkCa 8		< 6	< 0.7		< 10	< 0.5
9	IQ Tau		< 13	< 1.7		< 19	< 0.9
10	FX Tau		< 13	< 1.6		< 30	< 1.4
11	V710 Tau		< 12	< 1.5		< 7	< 0.4
12	DN Tau		< 9	< 1.2		< 20	< 1.0
13	CoKu Tau 3		< 7	< 1.0		< 16	< 0.8
14	CoKu Tau 4		< 18	< 2.2		< 20	< 1.0
15	BF Ori		< 300	< 36.7		< 275	< 13.5
16	RR Tau		< 26	< 3.2		< 192	< 9.5
17	IRAS 08267-3336		< 110	< 13.2		< 95	< 4.7
18	SX Cha		< 30	< 3.7		< 23	< 1.2
19	SY Cha		< 21	< 2.7		< 15	< 0.8
20	TW Cha		< 30	< 3.7		< 17	< 0.9
21	Ced 110 IRS6		< 35	< 4.4		< 22	< 1.1
22	B35		< 18	< 2.2		< 11	< 0.6
23	VW Cha		< 41	< 5.1		< 77	< 3.8
24	VZ Cha		< 30	< 3.7		< 27	< 1.4
25	WX Cha		< 14	< 1.8		< 21	< 1.0
26	ISO-Cha237		< 21	< 2.6		< 14	< 0.7
27	C7-11		< 14	< 1.7		< 10	< 0.5
28	HM 27		< 18	< 2.3		< 15	< 0.8
29	XX Cha		< 16	< 2.0		< 8	< 0.4
30	HD 98922		< 2300	< 280.8		< 14250	< 711.6
31	HD 101412		< 33	< 4.0		< 182	< 9.0
32	T Cha		< 3	< 0.4		< 4	< 0.2
33	IRAS 12535-7623		< 27	< 3.3		< 14	< 0.7
34	Sz50		< 23	< 2.9		< 18	< 0.9
35	ISO-ChaII 54		< 18	< 2.3		< 21	< 1.1
36	DL Cha		< 200	< 24.4		< 2250	< 111.7
37	HD 132947		< 0.1	< 0.0		< 3	< 0.2
38	HD 135344		< 45	< 5.6		< 42	< 2.1
39	HT Lup		< 39	< 4.9		< 65	< 3.2
40	HT Lup		< 64	< 7.9		< 107	< 5.3
41	GW Lup		< 5	< 0.6		< 4	< 0.2
42	Sz73		< 7	< 0.9		< 16	< 0.8

Table 5.3—Continued

#[a]	Source	$T_{\rm warm}$[b]	$N_{\rm warm}$[b]	$M_{\rm warm}$[b]	$T_{\rm hot}$[b]	$N_{\rm hot}$	$M_{\rm hot}$
			(r = 100 AU)[c]			(r = 2 AU)[c]	
		[K]	$[10^{22}{\rm cm}^{-2}]$	$[{\rm M_J}]$	[K]	$[10^{22}{\rm cm}^{-2}]$	$[10^{-3}{\rm M_J}]$
43	GQ Lup		< 4	< 0.5		< 18	< 0.9
44	IM Lup		< 15	< 1.9		< 25	< 1.3
45	RU Lup		< 44	< 5.5		< 87	< 4.4
46	RY Lup		< 35	< 4.3		< 45	< 2.2
47	EX Lup		< 20	< 2.5		< 24	< 1.2
48	Sz102		< 19	< 2.3	828	62	3.1
49	AS 205		< 62	< 7.7		< 185	< 9.2
50	Haro 1-1		< 6	< 0.8		< 13	< 0.7
51	Haro 1-4		< 6	< 0.8		< 23	< 1.2
52	DoAr 24E		< 26	< 3.3		< 97	< 4.8
53	SR 21		< 77	< 9.5		< 40	< 2.0
54	IRS51		< 38	< 4.7		< 18	< 0.9
55	SR 9		< 13	< 1.6		< 30	< 1.5
56	V853Oph		< 10	< 1.2		< 12	< 0.6
57	ROX42C		< 11	< 1.4		< 15	< 0.7
58	ROX43A		< 17	< 2.2		< 50	< 2.5
59	IRS60		< 7	< 1.0		< 42	< 2.1
60	Haro 1-16		< 12	< 1.4		< 24	< 1.2
61	Haro 1-17		< 8	< 1.1		< 4	< 0.2
62	RNO 90		< 48	< 5.9		< 102	< 5.1
63	Wa Oph 6		< 11	< 1.4		< 42	< 2.2
64	V1121 Oph		< 13	< 1.7		< 55	< 2.7
65	HD 163296		< 91	< 11.2		< 325	< 16.5
66	HD 163296		< 150	< 18.3		< 800	< 39.7
67	VV Ser		< 98	< 12.1		< 775	< 38.3
68	SSTc2d J182900.9		< 98	< 12.2		< 62	< 3.0
69	SSTc2d J182909.8		< 180	< 22.3		< 150	< 7.4
70	SSTc2d J182928.2		< 470	< 57.7		< 350	< 17.6
71	EC74		< 32	< 4.0	781	87	4.4
72	EC82		< 93	< 11.5		< 190	< 9.5
73	EC90		< 240	< 29.8		< 875	< 43.6
74	EC92		< 110	< 13.8		< 80	< 3.9
75	CK4		< 35	< 4.3		< 42	< 2.1
76	Lk Hα 348		< 57	< 7.0		< 1000	< 49.9

[a] Source number from Tables 5.1 and 5.2.

[b] If not specified, 100 K is assumed for the warm component and 1000 K for the hot component. The derived column density and mass of the warm component depend strongly on the assumed temperature. A temperature of 150 and 200 K reduces the column density and mass by respectively a factor of $\sim$ 30 and 140.

[c] Assumed emitting source sizes for the warn and hot component to estimate a column density.

Table 5.4. Summary of data for sources with detected H_2, [Ne II], or [Fe I] emission

#[a]	Source	log L H_2 S(2) [$L_\odot$]	log L H_2 S(3) [$L_\odot$]	log L [Ne II] [$L_\odot$]	log L [Fe I] [$L_\odot$]	log L IR [$L_\odot$]	T_{star} [K]	Age [Myr]	Class	log L_X [erg s^{-1}]
27	C7-11	< -5.5	–	< -5.6	-4.3	-2.1	4860	0.6	TTs	–
75	CK4	< -4.9	< -4.3	< -5.0	< -4.5	-1.6	4860	6.8	TTs	30.5
21	Ced 110 IRS6	-5.3	–	-5.2	< -4.8	-1.8	–	–	1	28.6
13	CoKu Tau 3	< -5.4	–	< -5.4	-4.6	-2.1	3800	–	CTTs	30.8
12	DN Tau	< -5.3	–	< -5.5	< -4.9	-2.1	3918	–	CTTs	30.1
52	DoAr 24E	< -4.7	–	< -4.8	< -4.6	-1.4	5160	2.0	TTs	29.8
71	EC74	-4.8	-4.0	-5.1	< -4.4	-1.9	–	–	2	30.5
72	EC82	-4.4	< -3.2	< -4.3	< -3.9	-0.9	3918	–	TTs	–
73	EC90	< -3.9	< -2.4	< -3.9	< -3.8	-0.3	–	–	TTs	31.0
74	EC92	-4.8	< -3.5	-4.6	< -4.2	-1.2	4273	–	TTs	–
37	HD 132947	< -6.2	< -5.2	< -6.4	-6.4	-3.2	10040	–	HAeBe	–
61	Haro 1-17	< -5.9	< -5.0	-6.0	-4.7	-2.6	3500	–	TTs	–
44	IM Lup	< -5.4	< -4.2	-5.4	< -5.0	-1.9	3918	0.7	TTs	–
7	IRAS 03446+3254	< -5.2	< -4.4	-4.9	< -4.3	-1.8	–	–	TTs	–
17	IRAS 08267-3336	< -4.5	< -3.9	-4.3	< -4.0	-1.1	5010	2.0	TTs	–
54	IRS51	< -5.4	–	< -5.2	< -4.9	-1.6	5570	0.8	2	30.9
59	IRS60	< -4.9	–	-5.1	< -5.0	-1.8	–	–	-	–
26	ISO-Cha237	< -5.5	–	< -5.2	< -4.6	-1.9	3918	–	TTs	29.2
2	Lk Hα 270	< -4.8	< -4.4	-4.7	< -4.4	-1.5	4273	0.01	TTs	–
3	Lk Hα 271	< -5.0	< -4.6	< -5.1	-3.7	-2.3	4860	–	TTs	–
16	RR Tau	< -4.8	< -3.7	-4.8	< -4.7	-1.4	–	0.6	HAeBe	–
53	SR 21	< -5.1	–	< -4.8	< -4.2	-1.2	6665	2.0	TTs	29.6
55	SR 9	< -5.2	–	-5.4	< -4.9	-2.0	4155	0.8	TTs	–
70	SSTc2d J182928.2	< -4.1	< -3.0	-3.6	–	-0.5	–	–	-	–
48	Sz102	-4.9	-4.1	-4.4	< -4.6	-2.2	3918	–	TTs	28.6
42	Sz73	< -5.4	< -4.9	-5.3	< -5.1	-2.1	3918	3.7	TTs	–
32	T Cha	< -6.0	–	-5.3	< -5.7	-2.8	5430	2.1	TTs	30.1
56	V853Oph	< -5.6	–	-5.2	< -5.1	-2.1	3800	0.8	TTs	–
23	VW Cha	< -4.8	–	-4.5	< -4.5	-1.6	4510	1.2	CTTs	31.0
25	WX Cha	< -5.3	–	< -5.3	-4.2	-1.9	4273	2.3	TTs	30.2
29	XX Cha	< -5.7	–	-5.4	< -4.6	-2.2	3800	14.6	TTs	–

[a] Source number from Tables 5.1 and 5.2.